Hypersonic Second-Mode Instability Response to Shaped Roughness

Andrew N. Leidy,[*] Rudolph A. King,[†] and Meelan M. Choudhari[‡]
NASA Langley Research Center, Hampton, Virginia, 23681

Pedro Paredes[§]
National Institute of Aerospace, Hampton, VA 23666

An experimental campaign was conducted on a 7 degree half-angle cone in the NASA Langley Research Center 20-Inch Mach 6 Wind Tunnel to examine the influence of arrays of regularly-spaced roughness elements on instability growth and transition. The primary element shape was a pair of elliptical planform ramps that were inclined at equal and opposite angles with respect to the local streamwise direction. The element shapes were designed to induce transient growth disturbances that would lead to sustained azimuthal modulation of the boundary layer flow while limiting the nearfield disturbances to avoid an immediate, i.e., effective tripping of the boundary layer. The bulk of the run matrix consisted of testing different element heights at freestream unit Reynolds numbers ranging from 9.8 to 13.1 million per meter. Other element shapes previously designed for tripping hypersonic boundary layers were also implemented. The model was instrumented with surface-mounted Kulite® and PCB® pressure transducers and thermocouples. Spectra from the PCBs® indicated clear suppression of the second-mode instability; however, neither the PCB® spectra nor the heat transfer data presented strong evidence for delayed turbulent flow. Complementary stability computations likewise demonstrated second-mode reduction, particularly just downstream of the roughness, but also revealed a rise in first-mode (streak-instability) amplitudes from the baseline that was likely responsible for the earlier transition observed for taller roughness cases.

Nomenclature

f	=	frequency	A	=	streak amplitude
m	=	azimuthal wave number	G_{xx}	=	autospectral density
p'	=	rms static pressure fluctuations	N_E	=	energy norm N-factor
p'_{tot}	=	rms static pressure fluctuations (10-1000 kHz)	Re	=	unit Reynolds number
p_s	=	model static wall pressure	St	=	Stanton number
x	=	axial distance from sharp nosetip	δ	=	boundary layer thickness

I. Introduction

BOUNDARY layer transition from laminar to turbulent flow presents significant challenges regardless of flight regime. Skin friction is the primary concern at lower speeds as early transition results in increased drag [1]. Thermal loading is crucial in hypersonics since heat transfer rates for turbulent boundary layers can be up to an order of magnitude higher than their laminar counterparts [2]. Flight vehicles must be designed to withstand worst-case loading, so uncertainties in heat transfer rates and transition location often lead to overdesigned, inefficient vehicles. Transition is governed by a number of variables including Mach number, freestream environment and flow quality,

---

model surface roughness and waviness, bluntness, cross-stream and streamwise curvature, pressure gradient, and temperature [3]. Pinpointing the predominant transition mechanism is critical for predicting where it will occur.

Boundary layer instabilities are typically studied on fundamental geometries to mitigate confounding variables. The second-mode instability is the dominant mechanism for transition on a sharp cone at zero degrees angle of attack in hypersonic conditions [4]. The instability is characterized by streamwise, acoustic waves trapped between the model wall and relative sonic line [5]. Several experimental studies [6–18] have been conducted on cones in hypersonic facilities within the past decade. Those tests were largely prompted by the novel utilization, in Ref. 19, of a piezoelectric dynamic pressure sensor that was originally designed for time-of-arrival applications. The PCB® has its limitations [20] but generally does provide a broad enough dynamic response to measure the high frequencies of the second-mode instability. Several of those recent campaigns examined the stabilizing effect of small nosetip bluntness on the second-mode instability and transition, while Ref. 8 included nosetips blunt enough to achieve transition reversal through another mechanism, similar to the results obtained by Softley [21] and Stetson et al. [22]. Marineau et al. [6] combined data from Ref. 8 with freestream noise measurements and linear stability theory computations to predict transition locations for geometries dominated by second-mode instabilities. Balakumar and Chou [23] incorporated freestream spectra from Ref. 7 into a DNS for the same cone tested experimentally at Mach 10 in Ref. 8. The computations indicated a transition location within 10% of the measured location on the sharp cone.

Adding surface roughness is a common method for tripping a boundary layer, but there have been some experimental studies [19,24,25] that have indicated delayed transition under the right conditions. Mechanisms for transition delay, in the presence of 2D roughness, were more thoroughly considered in the joint experimental and computational effort of Fong et al. [26]. Experiments from that study demonstrated delayed transition on a flared cone with several 2-D roughness strips positioned downstream of the synchronization location [27,28]. The present study, similarly, seeks to investigate computational findings pertaining to control of second-mode amplification via suitable azimuthal modulation of the basic state [29] through tests in Mach 6 flow on a 7 deg half-angle cone with elliptical planform shaped roughness elements. This paper provides surface pressure spectra and rms pressure fluctuation and Stanton number axial development plots for tests featuring elliptical roughness elements and other shapes to assess the effectiveness of shaped roughness in damping second-mode waves and delaying transition. Selected mean-flow computations and stability analysis are provided to complement the measurements.

II. Experimental Methods

A. The 20-Inch Mach 6 Tunnel
Tests were conducted in the NASA Langley Aerothermodynamics Laboratory (LAL) 20-Inch Mach 6 Tunnel. The tunnel is a conventional open-circuit blowdown-vacuum tunnel with planar nozzle contours that open into a nominally square test section. The infrastructural limits for testing are stagnation pressures between 207–3280 kPa and temperatures up to 555 K [30]. A recent campaign [31] characterized test section freestream fluctuation levels for unit Reynolds numbers between 3.28–26.5 million per meter (M/m). Mass flux fluctuations were relatively constant across the conditions, ranging from 1.8–2.5%, while pitot pressure fluctuations measured between 0.84–1.89%, decreasing with increasing Reynolds number [31]. For the present campaign, the total temperature was held at 484.3 ± 1.3 K and the total pressure was varied to achieve nominal freestream unit Reynolds numbers ranging from 9.8–13.1 M/m.

The tunnel was convectively preheated at the beginning of each day to promote thermal uniformity in the flow. Each run began by pulling a vacuum on the tunnel (vacuum spheres) and then opening the supply valves (high-pressure bottle fields). The tunnel was started without the testing article in the flow; the model was mounted on an injection plate in a bay below the test section while the tunnel was brought to the proper testing conditions. Once the targeted flow conditions were reached, the model was inserted into the flow with the model injection attitude control system outlined in Fig. 1. The model nosetip was centered in the test section and positioned 2.09 m downstream of the nozzle throat. The initial model wall temperature was 301.6 ± 2.2 K.

B. Test Model
The testbed for the present campaign was a 7 deg half-angle cone, composed of 15-5 stainless steel. The cone was segmented, which allowed for modularity and instrumentation. A sketch of the cone is provided in Fig. 2 with the segments represented by vertical lines. The sections used in the present campaign constituted the front 517 mm of the full 1.550 m model tested in Tunnel 9 [6-8] with additional sensors added prior to the present campaign. The nosetip piece was solid metal and had a 152 μm nose radius. The wall thickness of the aft two sections was 9.53 mm. Both of these sections were instrumented with surface-mounted PCB® 132B38 and Kulite® XCE-062-5D pressure transducers, type-E thermocouples, and static pressure ports. The PCB® sensors were powered using a PCB® signal conditioning

module, and built-in electronics high-pass filtered the output at 11 kHz. The differential Kulite® transducers were screenless to maximize frequency response and were all referenced to the single static pressure port identified in Fig. 2. The static sensitivities for the Kulites® were measured after installation of the Kulites® in the model. The distribution of sensors and other pressure ports along the 90 deg ray is sketched in Fig. 2. Kulites® were only located near the 90 deg ray, while the positions of PCB® transducers and thermocouples on the 0 deg and 180 deg rays are consistent with those on the 90 deg ray. The sensor cabling passed through the model sting and was run out of the tunnel to a centralized data collection rack.

The model was aligned by utilizing the static pressure ports located at x = 394 mm near each of the four cardinal rays. The model was estimated at $0 \pm 0.05°$ angle of attack and sideslip for the duration of the campaign.
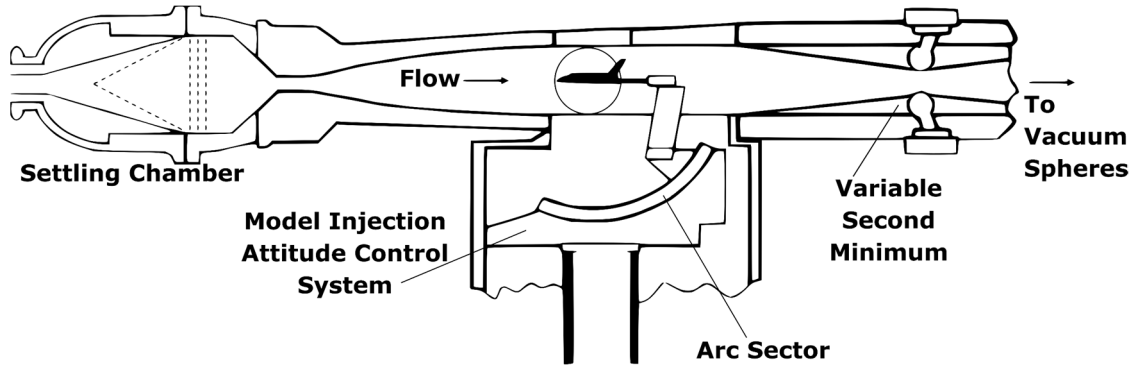

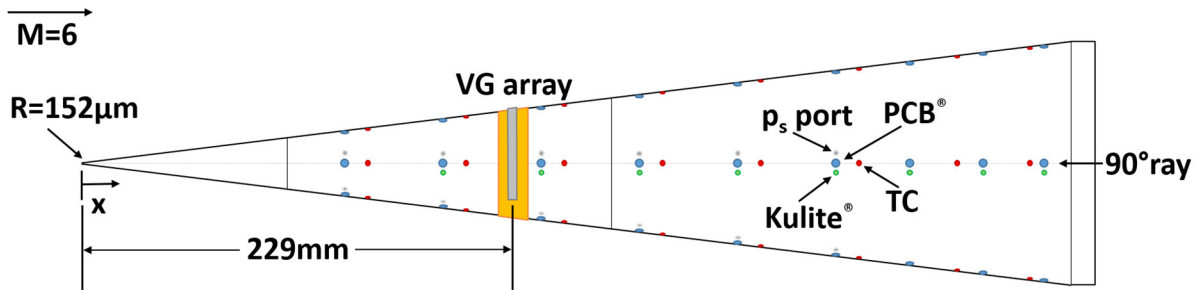**Figure 1. 20-Inch Mach 6 Tunnel schematic.**

Figure 2. Diagram of instrumented test article and relative position of roughness array.

The roughness consisted of an array of shaped elements that served as vortex generators (VGs). The elements were designed based on the lessons learned from Ref. 29, and the parameters scaled with the estimated ($U/U_e = 0.995$) boundary layer thickness $\delta = 1.1$ mm at x = 229 mm for Re = 9.8 M/m. Each wavelength consists of a pair of elliptical planform elements that are rotated 3.017 deg relative to the streamwise direction. The optimal wavelength, semimajor axis, frontal width, and height are all functions of the boundary layer thickness. Measured parameters for the elliptical arrays are listed in Table 1. The measured wavelength of 1.584 mm is equivalent to an azimuthal wavenumber of ~112. Similar wavelength, length, and height dimensions were chosen for the triangular and trapezoidal arrays.

Each array was 3-D printed as a single piece using a polyjet process with a stated resolution of 14 μm. The material was known as Agilus30, which had a Shore 95A hardness and a rubbery feel. The part consisted of a base layer that was nominally 150 μm thick. The VGs were printed 5 mm downstream of the leading edge of the part to allow the boundary layer to recover from the initial forward facing step. The centers of the elements were positioned 229 mm downstream of the nosetip as shown in Fig. 2. The printed strip continued downstream of the elements for a total part width of 15 mm. The part azimuthally spanned 270 degrees, with roughness elements distributed between 45 and 225 degrees on the base layer. Adhesive transfer tape (nominally 58 μm thick) was applied to the back of the printed piece

to secure it to the cone surface. A photograph of a VG array consisting of elliptical planform elements along with some downstream instrumentation is shown in Fig. 3. The heights of the forward facing and rearward facing steps were consistently measured near 200 µm. Additional information regarding the roughness elements is depicted in Fig. 4. Two wavelengths of each roughness shape are sketched in the upper left of the figure. The upper right displays a segment of an elliptical roughness array. Sample measured topographical maps of two wavelengths for each roughness shape are presented at the bottom of Fig. 4. The mean height for the array is noted on each map. The white outlining ellipse surrounding the top roughness is the designed footprint of that element. The footprint demonstrates that the print and designed shapes compare favorably, although there is some rounding on all edges.

Table 1. Elliptical roughness design parameters.

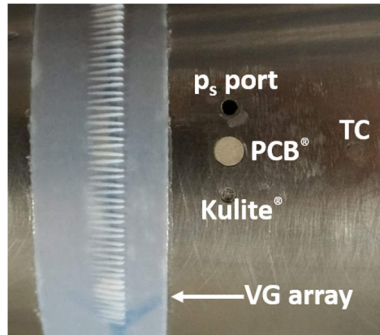| Parameter	Measured Value
Wavelength (λ)	1.584 mm
Semi-major axis (a)	1.74 mm (from ht: 0 to peak) 2.05 mm (from ht: 0 to 0)
Semi-minor axis (b)	0.13 mm (at 75% height)
Aspect Ratio	13.4
Height (k)	Varied (see Table 2)

Figure 3. Elliptical planform VG array and downstream instrumentation near the 90° ray.

Each roughness array was individually scanned using a 3-D measuring macroscope. The scans were conducted in high-magnification mode at 40x, with a resolution of 7.3994 µm per pixel and a measured height accuracy of ± 3 µm. The scanner post-processing software was used to level the image by setting the array base as the reference. The stated element height was characterized using the following process. Spanwise profiles were generated across the elements for all streamwise positions. To further correct for sample leveling, a second-order mean function was removed from each profile, centering it at zero height. The profile with the highest mean peak-to-valley height defined the height of the roughness. In this study, six elliptical element arrays were tested, along with one triangular and one trapezoidal. The mean and standard deviation of the element heights are denoted in Table 2. The cone was also tested in a baseline configuration without a strip and, additionally, was tested with a blank strip (base layer) containing no roughness elements (a planform with nominal 200 µm forward and backward steps).
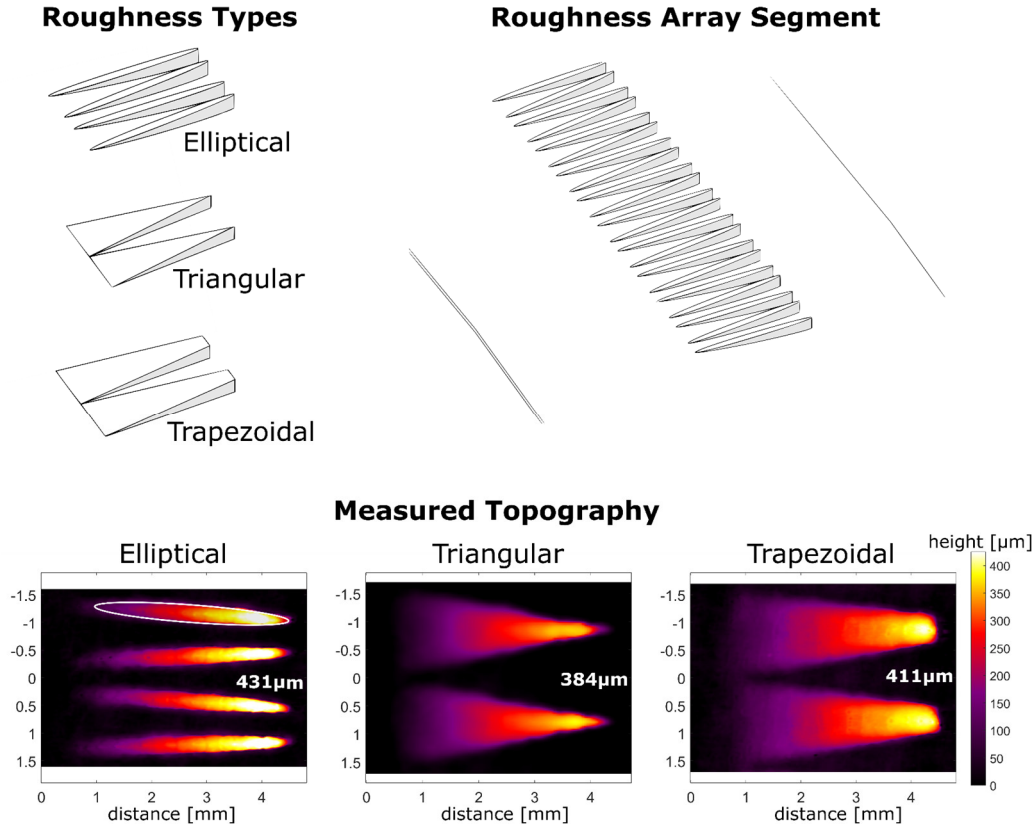
Figure 4. Roughness element summary. Sketches of elliptical, triangular, and trapezoidal element shapes (upper left), a sketch of a segment of an elliptical roughness array (upper right), and measured topographical maps of roughness elements (bottom).

Table 2. Roughness element peak-to-valley height.

Element shape	Mean (μm)	Standard deviation (μm)
Elliptical	235.2	18.3
Elliptical	381.2	21.3
Elliptical	430.7	21.2
Elliptical	455.3	20.4
Elliptical	470.2	21.0
Elliptical	528.6	16.8
Triangular	384.2	12.1
Trapezoidal	410.9	17.2

C.   Data Acquisition and Processing

The data acquisition system was triggered after model injection, once the model reached the tunnel centerline. The thermocouples were sampled immediately, while sampling of the PCBs® and Kulites® began one second later. The thermocouples were sampled at 25 kHz for 3 seconds and were low-pass filtered at 2 kHz. The PCBs® were sampled at 2.5 MHz for 2 seconds, high-pass filtered at 100 Hz, and low-pass filtered at 1 MHz. The Kulites® were sampled at 500 kHz for 2 seconds, high-passed at 100 Hz, and low-passed at 100 kHz to mitigate the effect of the resonance peak. The mean flow conditions and static pressures were sampled at 20 Hz by the tunnel DAS, which followed the same trigger. The reported flow parameters were calculated by the facility using GASPROPS [32]. That code incorporates real gas effects, following a multiple-coefficient virial equation of state. The compressibility factor ranged from 1.0039–1.0053 for conditions tested herein. It also uses the Chapman-Cowling viscosity model, which includes

Lennard-Jones potentials. The resulting unit Reynolds numbers compare favorably with those computed using Keyes viscosity for the static temperatures tested.

The power spectral density (PSD) was estimated using Welch's method [33]. Hamming windows of 12,500 points and 2500 points for PCBs® and Kulites, respectively, with 50% overlap were averaged to yield the PSD. These parameters result in a frequency resolution of 200 Hz, with random error in PSD value of under 4%. The response function of PCB® transducers is unknown, but spurious spectral content, notably near 300 kHz, is often attributed to the sensors. The factory-provided sensitivity calibration is based on a single pressure test point [20]. Therefore, significant uncertainties are present in both the root mean square (rms) pressure fluctuation levels and at PSD values for a given frequency. Corrections to the factory calibration were made for PCBs® along the 90 deg ray. Kulites® are in close proximity to PCBs® on the 90 deg ray, with Kulites® azimuthally shifted off the ray by about 4.8 mm. Therefore, rms values over the frequency range of 30–80 kHz were matched for each sensor pair to provide better PCB® PSD estimates. Only the eight total runs without VGs were considered for this correction. The mean and standard deviation of each PCB® to Kulite® rms ratio are given in Table 3. Five of the eight mean ratio values are within ±10% of unity, meaning that the stated PCB® calibrations were fairly accurate. A significant exception is the final PCB® on the ray, where the stated sensitivity was roughly 50% higher than was measured by the neighboring Kulite®. The corrected PCB® values are documented in this paper.

Frequencies between 10 kHz and 1 MHz and between 100 Hz and 100 kHz for PCBs® and Kulites®, respectively, were considered in the calculation of rms pressure fluctuations.

Table 3. PCB®/Kulite® rms (30-80 kHz) pressure fluctuation ratio.

x-location (mm)	Mean	Standard deviation
190.5	1.1034	0.0111
241.3	1.0303	0.0163
292.1	0.9721	0.0147
342.9	1.1775	0.0396
393.7	1.0763	0.0299
431.8	1.2413	0.0263
469.9	1.0702	0.0053
501.7	1.5155	0.0041

The time-varying surface heat flux was estimated using a numerical code that solves the 1-D heat conduction equation using the cylindrical coordinate method outlined in Ref. 34. At each thermocouple, 50 nodes were specified and equally-spaced radially through the 9.53 mm thickness of the material, and the time history of temperature was estimated at each node. The boundary conditions were provided by the surface thermocouple and an interior thermocouple. The heat flux was calculated by estimating the temperature gradient near the surface from the temperature values of the three nodes closest to the surface. The heat flux was calculated assuming the thermal properties of the constantan thermocouple rather than the stainless steel model. The thermal diffusivity of 15-5 stainless is 13% less than that of constantan, which amounts to a less than 4% reduction in Stanton number. Stanton number was the nondimensional heating parameter of choice since it normalizes the heat flux by the freestream mass flux to mitigate potential bias due to variations in unit Reynolds number. Here, the Stanton number is defined as

$$St = \frac{Q}{\rho_\infty u_\infty c_p (T_0 - T_w)} \tag{1}$$

where Q is the heat flux, ρ_∞ is the freestream density, u_∞ is the freestream velocity, and c_p is the specific heat of the flow. The temperature difference is between the tunnel total temperature and the model wall temperature, which did not increase much during the three-second runs. The largest measured wall temperature increase was 2.4 deg C.

There was considerable scatter in some raw temperature time series due to electronic noise. The uncertainty bars plotted herein account for the uncertainties in the material properties and for the spread in the temperature data.

III.   Experimental Results

A.   Smooth Cone

Baseline runs were conducted on the smooth cone at the three unit Reynolds numbers of interest: 9.8, 11.5, and 13.1 M/m. Convective surface heating generally provides definitive information regarding transition. The onset of transition is characterized by the initial, precipitous rise in heating; the end of transition is near the peak heating [3]. The influence of the freestream Reynolds number on the transition location for the smooth cone is shown in Fig. 5. Note that the 0 deg ray has the most operational thermocouples, followed by the 90 deg ray and then the 180 deg ray. Unfortunately, there are very few thermocouples in the vicinity of the transition region at the Reynolds number of interest. Thus, the thermocouple at 202 deg will be used to supplement the 180 deg measurements based on their azimuthal proximity. The axial development of Stanton number suggests slightly earlier transition on the 90 deg ray. For example, transition onset at Re = 9.8 M/m on the 0 deg ray occurs near x = 406 mm (Fig. 5a). However, onset occurs farther upstream on the 90 deg ray since the Stanton number is already elevated at x = 406 mm. Transition onset advances upstream by roughly one sensor station (50.8 mm) for each increase in unit Reynolds number.
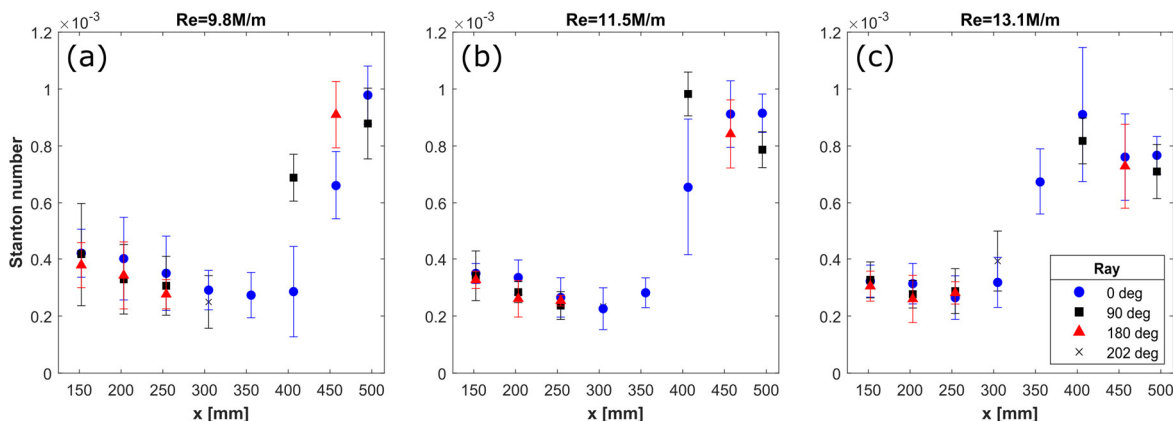

Figure 5. Axial development of Stanton number along the smooth cone for three unit Reynolds numbers (a-c).

PSD plots of pressure fluctuation from the two primary rays considered herein, 90 deg and 180 deg, are shown in Fig. 6. The 90 deg plot (Fig. 6a) contains composite PSDs from both Kulite® and PCB® data plotted over frequency ranges of f < 80 kHz and f > 40 kHz, respectively. Both the magnitude and the slope of the PSDs demonstrate good agreement for the range of overlapping frequencies. While the peak PSD amplitude in the range of second-mode frequencies occurs at x = 292 mm on the 90 deg ray, the PCB® rms integrated over all frequencies attains its highest value at x = 343 mm and is 12.5% higher than the value at x = 292 mm, due to a similar second-mode amplitude and considerably more content at lower frequencies. This is the spectral broadening that occurs as the second mode saturates. Farther downstream, the spectral hump associated with the second-mode instability is nearly gone by x = 394 mm, and the spectra appear turbulent thereafter. The 90 deg PCB® and Kulite® spectra convey a trend for locations downstream of the maximum second-mode amplitude (x ≥ 394 in Fig. 6a). Spectral energy decreases for frequencies below 200 kHz as the streamwise position increases. Though not pictured here, this trend is not observed in the 90 deg PCB® spectra without considering calibration corrections. It is, however, corroborated by the corresponding spectra on the 180 deg ray (Fig. 6b), suggesting that the manufacturer-provided PCB® calibrations on the 180 deg ray are more consistent than those on the 90 deg ray. The power spectra for the 180 deg ray also demonstrate that transition occurs slightly further downstream compared to the 90 deg ray. A clear maximum in the second-mode peak occurs at x = 343 mm, meaning the difference in transition onset between rays is less than the axial spacing of consecutive sensors (50.8 mm). A second-mode peak is still present at x = 394 mm, but spectra downstream of that point all appear turbulent.
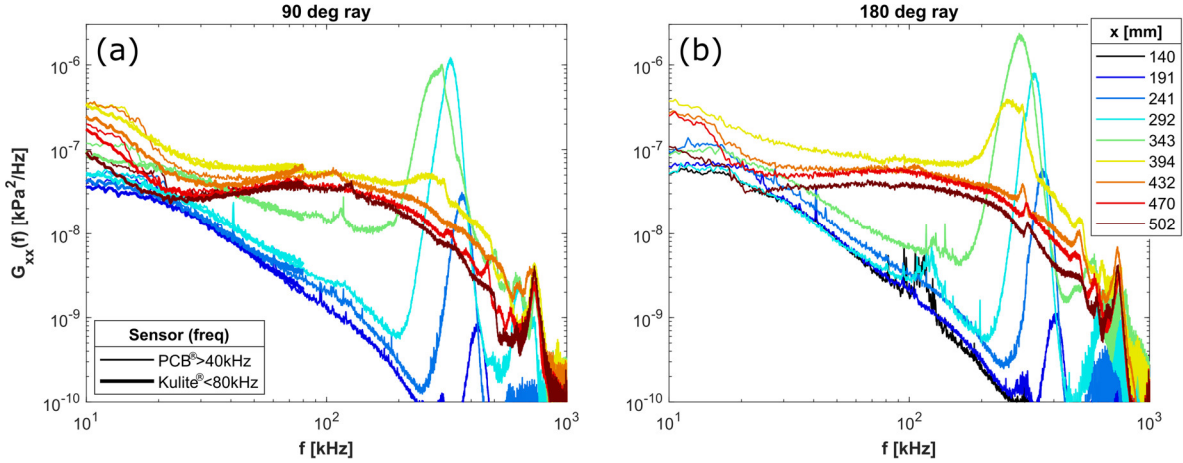
Figure 6. PSD plots of pressure fluctuations on the smooth cone at Re = 11.5 M/m, measured on the (a) 90° and (b) 180° rays. The 90° ray plot includes PSDs from both Kulite® and PCB® sensors.

Figure 7a depicts the axial development of rms pressure fluctuations normalized by the static pressure on the surface of the cone, which was calculated for each run using Taylor-Maccoll relations. These profiles also suggest later transition on the 180 deg ray for all three unit Reynolds numbers of interest, with maximum PCB® rms values for the 180 deg ray occurring at or downstream of corresponding maximum values on the 90 deg ray. The differences in rms profiles between rays appear to become less as the Reynolds number increases, but that observation may be a consequence of the relatively wide sensor spacing. The 90 deg Kulites®, depicted as the filled squares, initially rise in amplitude near the same axial location that the PCBs® reach a maximum rms value. A decreasing PCB® rms and an increasing Kulite® rms physically represents the redistribution of energy from the second-mode instability to lower-frequency disturbances. That spectral shift can be better visualized in Fig. 7b, where the second-mode and lower-frequency content are each plotted as a fraction of the full PCB® spectral (total) rms. The lower-frequency bound of the second-mode instability peak was defined as the local minimum PSD value to the left of the peak; the higher-frequency bound was defined as the frequency having the same PSD value on the right side of the peak. The lower-frequency content was from 10 kHz to the lower bound of the second mode or to 100 kHz if a second-mode peak was not detected. The second-mode fraction is denoted by the same symbols as in Fig. 7a, while the lower-frequency fraction uses the same symbols but are outlined in black. Although the second mode is detected at the most upstream sensors, the bulk of the energy is in the lower frequencies for x ≤ 191 mm. The second mode dominates farther downstream, with the highest second-mode fraction corresponding with the same location as the highest total rms. The lower frequencies fill in as the second mode saturates, and the second mode can no longer be detected one or two stations downstream of its peak value. At the end of the cone, the lower-frequency (10–100 kHz) fraction of the total (10–1000 kHz) rms converges to a value just above 0.6.
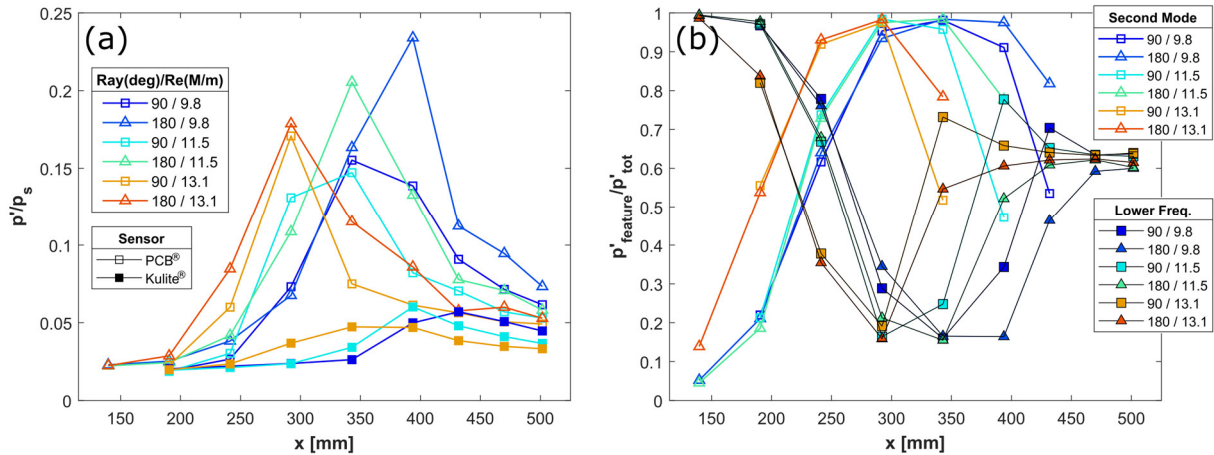
Figure 7. Axial development of (a) rms pressure fluctuations on the smooth cone along 90° and 180° rays, with both Kulites® (100 Hz – 100 kHz) and PCBs® (10 kHz – 1 MHz) considered for the 90° ray and (b) second-mode and lower-frequency rms as a fraction of full PCB®-bandwidth rms.

It is instructive to compare the Stanton number evolution (Fig. 5) with the PSD plots (Fig. 6) and rms pressure fluctuation curves (Fig. 7). These sets of data indicate that the onset of transition is characterized by an initial filling of the frequencies below the second-mode peak on the PSDs, which occurs when the rms pressure fluctuations from the Kulites® initially rise and the rms PCB® fluctuations reach a peak. The end of transition corresponds to the collapse of the spectra at different axial stations into a similar shape, the Kulite® rms reaching a maximum, and the most upstream point that matches the slope of all turbulent downstream points in the PCB® rms profile. These correlations will prove particularly useful in Section III.B below, where we analyze the effects of the roughness element arrays on the disturbance evolution and the transition characteristics over the cone. Since the observed shifts in the transition onset location are relatively modest, i.e., comparable to the axial spacing between the thermocouples, the data assimilation based on the unsteady pressure sensors helps us partially compensate for the sparsity of the thermocouple measurements.

B. Elliptical Roughness

Tests were conducted using arrays of elliptical elements of six different heights. The axial development of Stanton number for the three unit Reynolds numbers on the 90 deg ray is plotted in Fig. 8. Despite the lack of spatial resolution and sensors in the transition region, important information can be gathered. The roughness array is centered between the second and third thermocouple stations. At each Reynolds number, the Stanton number decreases between the first and second thermocouple for all VG configurations, indicating that the flow leading into the roughness array is laminar. Differences in heating are observed downstream of the VGs depending on the element height. The tall (≥ 431 µm) elements indicate an increase in Stanton number, whereas the Stanton number continues to decrease across the VG array for shorter heights. A couple of exceptions to this trend are observed for the Re = 13.1 M/m case (Fig. 8c), where the Stanton number actually increases for the baseline and blank array cases, but decreases for the 235 µm and 381 µm height elliptical roughness. The PSDs for those specific cases are examined later in this subsection. The fourth station (x = 406 mm) in Fig. 8 generally reflects a maximum Stanton number, which means the end of transition is at or near that location. Re = 9.8 M/m presents some exceptions where the flow is clearly still transitional at x = 406 mm since the Stanton number is still increasing up to the final location for the baseline case (i.e., no VGs) as well as for the shorter VG arrays.
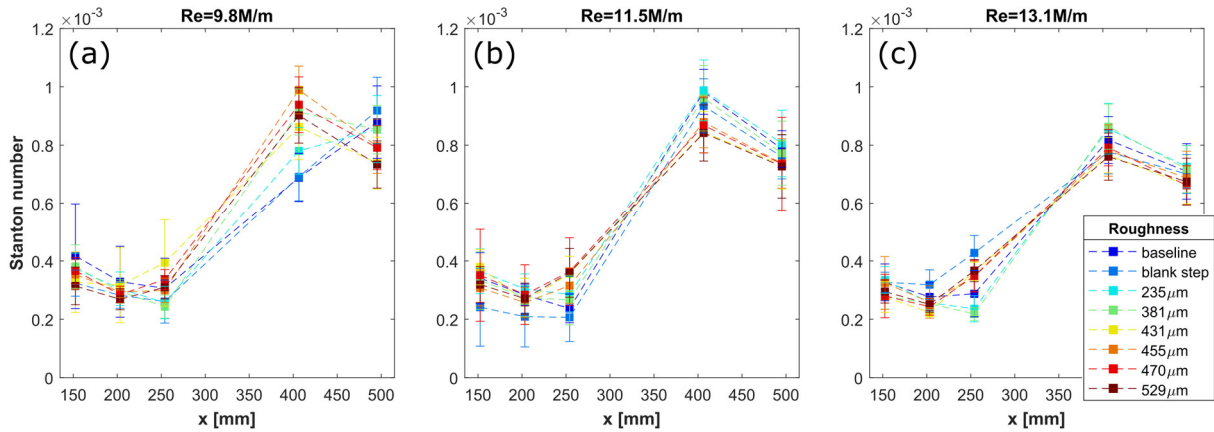
Figure 8. Axial development of Stanton number along the 90° ray for three unit Reynolds numbers (a–c) and six VG heights.

Spectra from the four 90 deg ray PCB® and Kulite® sensors positioned just downstream of the roughness strip and tested at Re =11.5 M/m are presented in Fig. 9. The second-mode instability is strongest when there is no roughness present. The blank, 200 micron step does not have a significant impact on the amplitude of the second-mode peak at these conditions, but it does contribute to growth at frequencies just below the second-mode peak. The presence of the step associated with the blank leads to elevated disturbance amplitudes in comparison to the baseline case for the sensors at x = 241 mm (Fig. 9a) and x = 292 mm (Fig. 9b). Farther downstream (x ≥ 343 mm), the spectra with the blank are nearly identical to those in the baseline case. It should be noted from Fig. 6a that the baseline spectrum at lower frequencies (i.e., below the second mode lobe) is already elevated by x = 343 mm, meaning that the onset of transition has occurred for all heights by this streamwise station at Re = 11.5 M/m. The VGs significantly affect the disturbance growth at second-mode frequencies. The sensors at x = 241 mm are located 12.7 mm downstream of the center of the roughness array. All second-mode amplitudes are significantly reduced, and the frequency corresponding to the peak PSD within the second mode range is also shifted lower by nearly 60 kHz from the baseline peak (Fig. 9a). The x = 292 mm station (Fig. 9b) indicates that the second-mode amplitude progressively decreases with an increasing height of the elliptical roughness elements.

Also observed, primarily in Fig. 9b, is the discrepancy between some overlapping Kulite® and PCB® spectra. Specifically, the spectra measured by the two sensor types do not match within the overlap range of 40 kHz to 80 kHz for the three tallest VG arrays. However, this discrepancy is believed to be an artifact of the azimuthal variations in the disturbance amplitudes from the 90 deg ray of PCBs® to the 4.8 mm surface distance offset of the Kulites®, rather than being caused by any inconsistencies in the calibration process. The taller VGs also lead to increased PSD values at frequencies just below the second-mode lobe at both x = 241 mm and x = 292 mm, similar to changes in the PSD due to the blank step; however, the elevated lower-frequency content for the taller roughness heights does not return back to the level of the baseline case. The additional lower-frequency content may be the result of first-mode excitation. Numerical studies have shown that the first mode can become the streak instability disturbances of the three-dimensional modulation induced by the roughness elements and experience a destabilization that depends on the streak amplitude [35]. The spectra at x = 343 mm (Fig. 9c) indicate two different kinds of behavior depending on the VG height. The cases with a VG height of 381 μm or lower exhibit similar spectral content below 150 kHz, whereas VGs with a height of 431 μm and above lead to elevated spectral content at those frequencies. Surface pressure spectra for taller VGs already appear to be turbulent at x = 343 mm. By x = 394 mm (Fig. 9d), all spectra are close to turbulent.

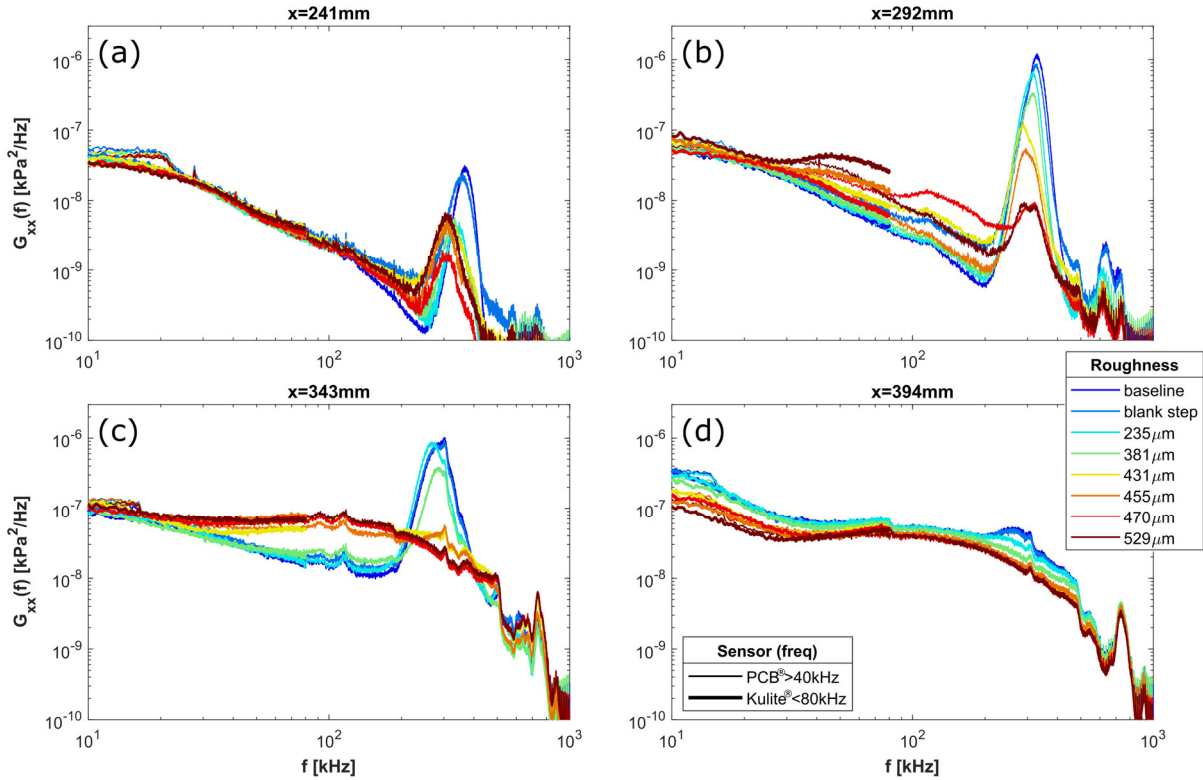American Institute of Aeronautics and Astronautics

Figure 9. PCB® and Kulite® pressure fluctuation spectra at four streamwise stations (a–d) on the 90° ray for six elliptical roughness heights at Re = 11.5 M/m.

As previously mentioned, the Stanton number values for Re = 13.1 M/m in Fig. 8c suggest some irregularities regarding the 235 µm and 381 µm VGs compared to the other data. The Re = 13.1 M/m spectra at x = 292 mm (Fig. 10a) show that the lower-frequency content for these two short VG heights is less than the baseline and blank array cases, just as the Stanton number values are less at x = 254 mm. This suggests that the onset of transition may be delayed for the 235 µm and 381 µm VGs but may also be a consequence of the azimuthal variation in forcing. The PSDs farther downstream, at x = 343 mm (Fig. 10b), show that the flow is turbulent for most VG heights. However, it appears that the 235 µm elliptical roughness height is slightly further from the similar PSD turbulent shape than the blank case, which suggests transition to fully turbulent flow may be slightly delayed. The intermediate Re = 12.3 M/m spectra (not pictured here) also demonstrate this finding.
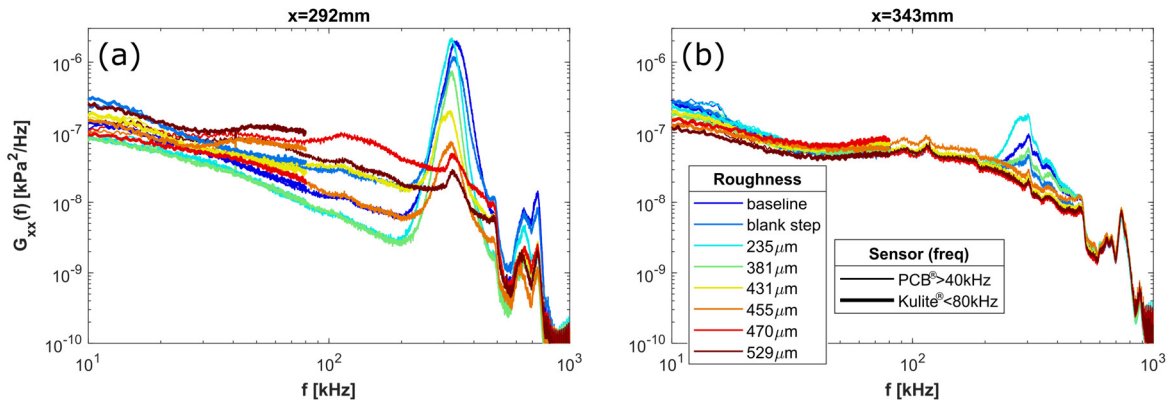

Figure 10. PCB® and Kulite® pressure fluctuation spectra at two locations (a,b) on the 90° ray for six VG heights at Re = 13.1 M/m.

The axial development of rms pressure fluctuations along the 90 deg ray is plotted in Fig. 11. The decrease in PCB® pressure fluctuation magnitude with increasing VG height is observed for all three unit Reynolds numbers. At a given Reynolds number, the maximum fluctuation level is measured near the same axial location regardless of the VG height, with some exceptions where the maximum rms is recorded by the sensor located immediately downstream (see Fig. 11c). The downstream shift in peak amplitude in the latter cases is attributed to the observation that the second-mode amplitude is so far reduced that broad, elevated content at frequencies below the second mode is the principal contributor to the rms fluctuations. The Kulite® transducers indicate that the lower-frequency pressure fluctuations for the taller VGs often rise and reach a maximum value farther upstream than shorter VG or no roughness cases. However, comparatively higher lower-frequency fluctuation levels are noted for the shorter VGs once turbulence is achieved. The PCB® rms values at the three stations farthest downstream are similar for VGs shorter than 381 µm, indicating a similar location for the start of fully turbulent flow between the configurations for each respective Reynolds number.
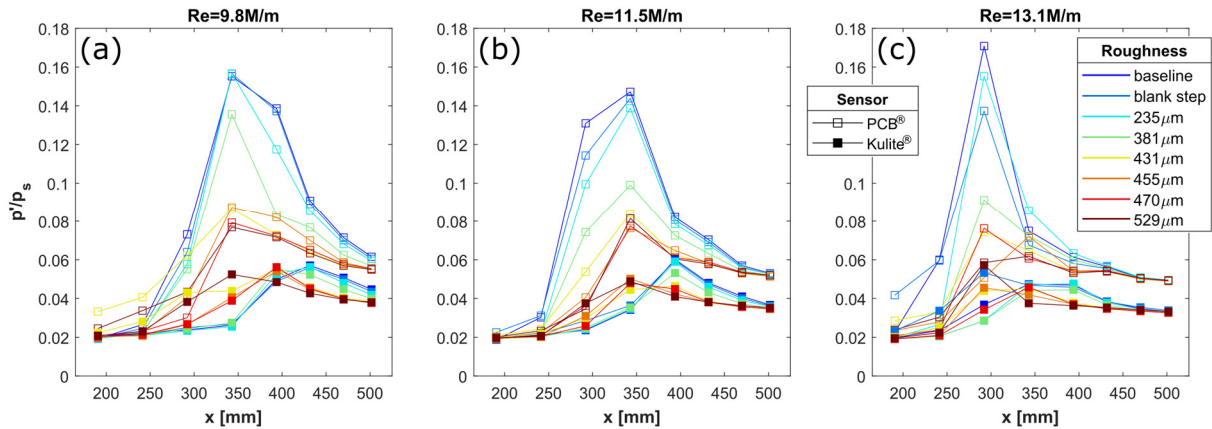

Figure 11. Axial development of rms pressure fluctuations from PCB® and Kulite® sensors along the 90° ray for three unit Reynolds numbers (a–c) and six VG heights.

Lower-frequency and second-mode instability pressure fluctuation profiles for the 90 deg ray are plotted in Fig. 12. Lower-frequency points below x = 292 mm are omitted from the plots for clarity since the lower-frequency curves have high values near the front of the cone (see Fig. 7b) and would cross over the second-mode curves. The growth in the second mode between the two most upstream stations (x = 191 and x = 241 mm) is significant for the baseline case for all unit Reynolds numbers. The relative second-mode growth rate is reduced from the baseline when comparing across the VGs, with the slope tending to decrease for increased VG height. The second-mode instability growth picks up for the shorter roughness heights between x = 241 mm and x = 292 mm but does not recover for the tallest elements (470 and 529 µm), where much of the energy is concentrated in the lower-frequencies over the full length of the cone. The redistribution of energy from the second mode to the lower frequencies is similar for heights ≤ 381 µm. The turbulent fraction of lower-frequency rms to total rms is just above 0.6 for all cases.
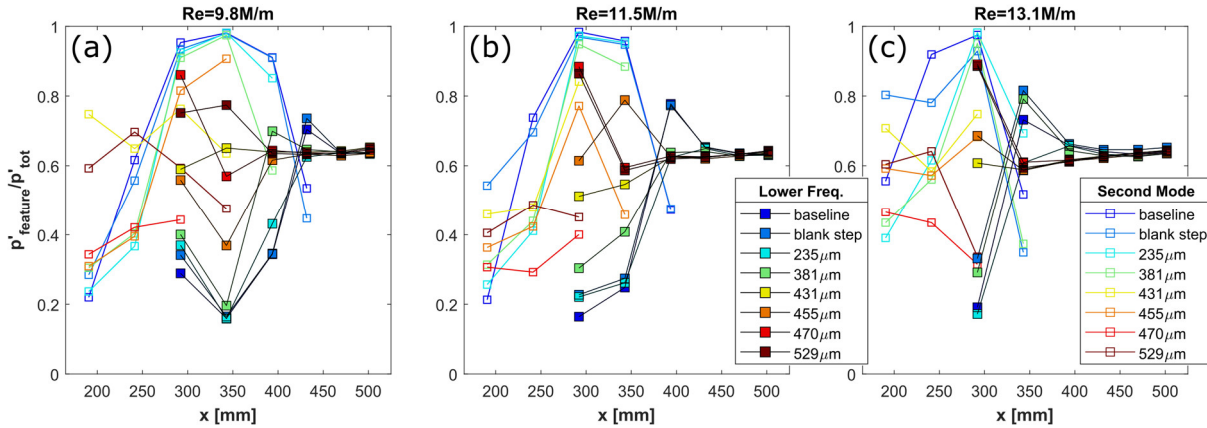
Figure 12. Axial development of second-mode and lower-frequency rms as a fraction of full PCB®-bandwidth rms along the 90° ray for three unit Reynolds numbers (a–c) and six VG heights.

Similar analysis can be made for data taken along the 180 deg ray, which was shown in Section IIIA to transition slightly farther downstream compared to the 90 deg ray. The axial development of the Stanton number for thermocouples near the 180 deg ray is plotted in Fig. 13. Again, the flow is laminar coming into the VGs, and the taller roughness elements tend to elevate the Stanton number the most between x = 203 mm and x = 254 mm. The fourth station (x = 305 mm) on the Stanton number plot was measured at 202 deg, which is expected to give similar results as the points located on the 180 deg ray. Some of the Stanton number values actually decrease for the taller VGs between x = 254 mm and x = 305 mm, suggesting some azimuthal dependence, i.e., the potential that the upstream thermocouple is located under a wake that brings higher energy flow close to the surface. The Stanton number for the 235 μm VGs, similar to the 90 deg ray, breaks the trend directly behind the roughness for the Re = 13.1 M/m case, where it continues to decrease in Stanton number while all other configurations increase (Fig. 13c). The Re = 13.1 M/m spectra (not shown here) indicate lower-frequency PSD values for both the 235 and 381 μm heights that are below the baseline case at the x = 292 mm and x = 343 mm locations. The 529 μm case is clearly the most transitional at x = 305 mm for all three Reynolds numbers. Its Stanton number values are far above the other cases, and the value is near the anticipated maximum value (St = 1.0 x 10⁻³) for Re = 13.1 M/m, meaning the flow is already near the end of the transitional stage.
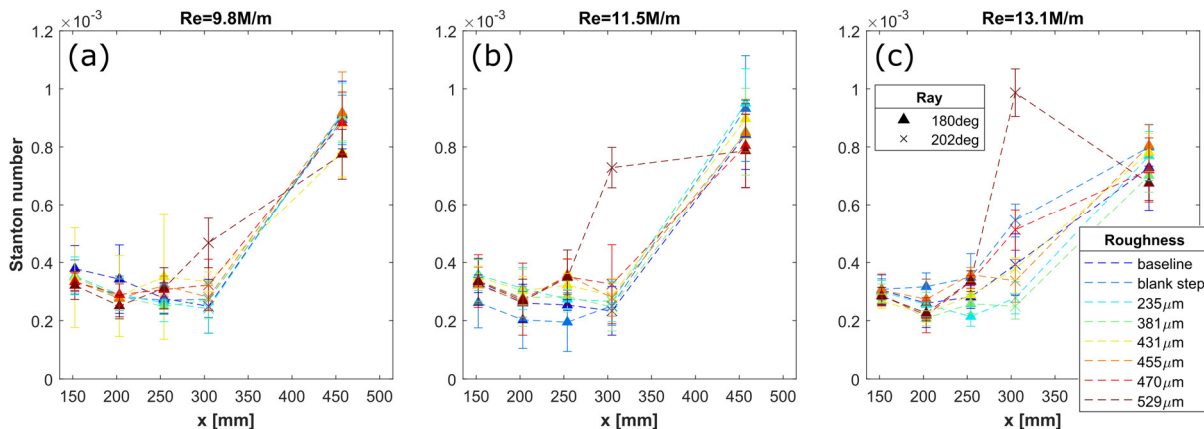

Figure 13. Axial development of Stanton number, computed using thermocouples near the 180° ray for three unit Reynolds numbers (a–c) and six VG heights.

Spectra from PCB® sensors along the 180 deg ray for Re = 11.5 M/m are presented in Fig. 14. Similar trends that were noted for the 90 deg ray are observed here. There is a progressive reduction in second mode amplitude and shift to lower frequencies for increasing VG height at x = 241 mm (Fig. 14a). The transition process appears to lag comparatively behind the 90 deg ray for all roughness heights, except for the 455 µm case, which may again be due to relative azimuthal positioning. At x = 343 mm (Fig. 14c), the spectra can be divided into two groups based on roughness height, with the 381 µm VGs caught between groups. The spectra for the 381 µm case still demonstrate a significant reduction in the second mode, while maintaining lower-frequency spectral content near the baseline level. By x = 394 mm (Fig. 14d), roughness heights 381 µm and taller are turbulent, while the 235 µm, blank, and baseline cases still have content above the similar turbulent PSD curve.

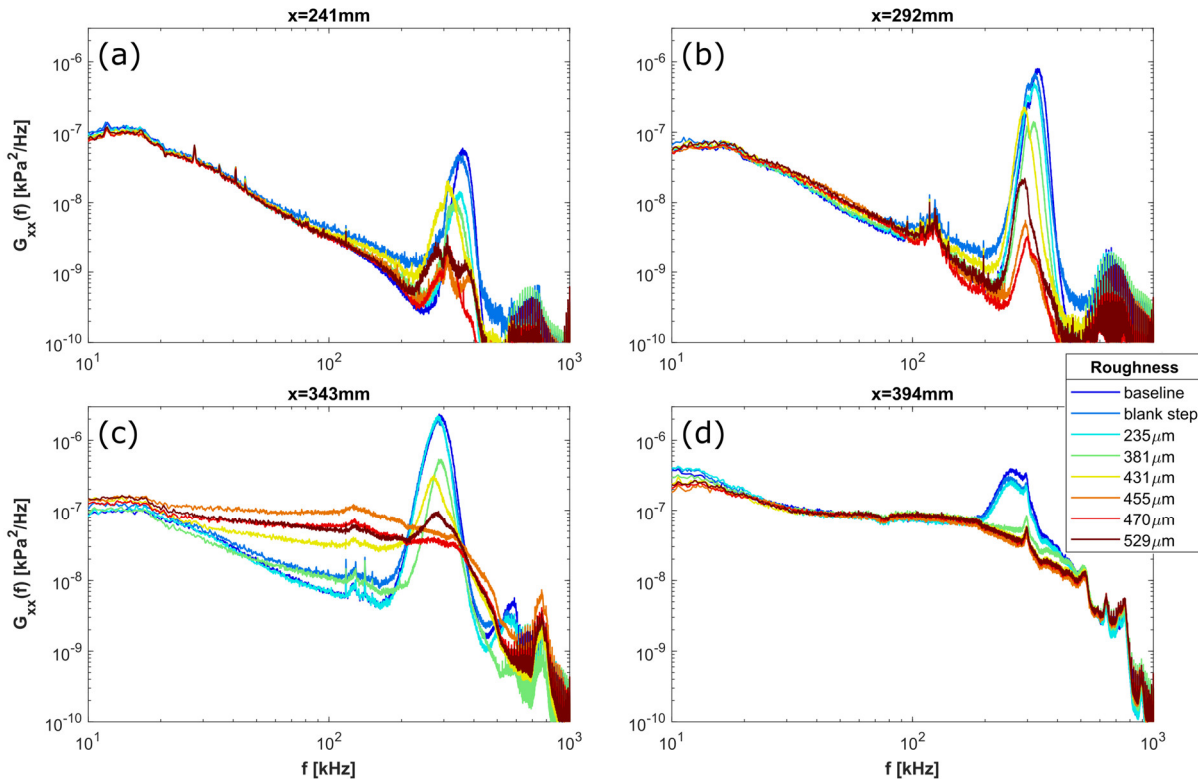**Figure 14. PCB® pressure fluctuation spectra at four streamwise stations (a–d) on the 180° ray for six elliptical roughness heights at Re = 11.5 M/m.**

The rms fluctuations measured by the PCBs® on the 180 deg ray for three Reynolds numbers are given in Fig. 15. The most notable differences between these plots and the plots for the 90 deg ray (Fig. 11) are that the peak rms values occur one station farther downstream for some cases and that the maximum rms values are higher on the 180 deg ray, which could potentially be attributed to the PCB® factory calibrations since this was also observed in Fig. 7a. The rms fluctuations at Re = 11.5 M/m (Fig. 15b) corroborate observations made using the spectra in Fig. 14. That is, the fluctuation levels, which are largely dictated by the amplitude of the second-mode peak, tend to decrease as the roughness height increases. The relative fluctuation reduction due to the roughness is more significant on this ray compared to the 90 deg ray, which leads to more examples of the rms peaks for tall VGs occurring downstream of rms peaks for short VGs. Again, this is not an indication of delayed transition onset like it was for the baseline case in Section IIIA. The reason the peak rms occurs farther downstream for tall VGs is because the second-mode amplitude is greatly reduced and the lower-frequency content is responsible for the peak. For these cases, the rms peak no longer represents the onset of transition; it represents fully turbulent flow.
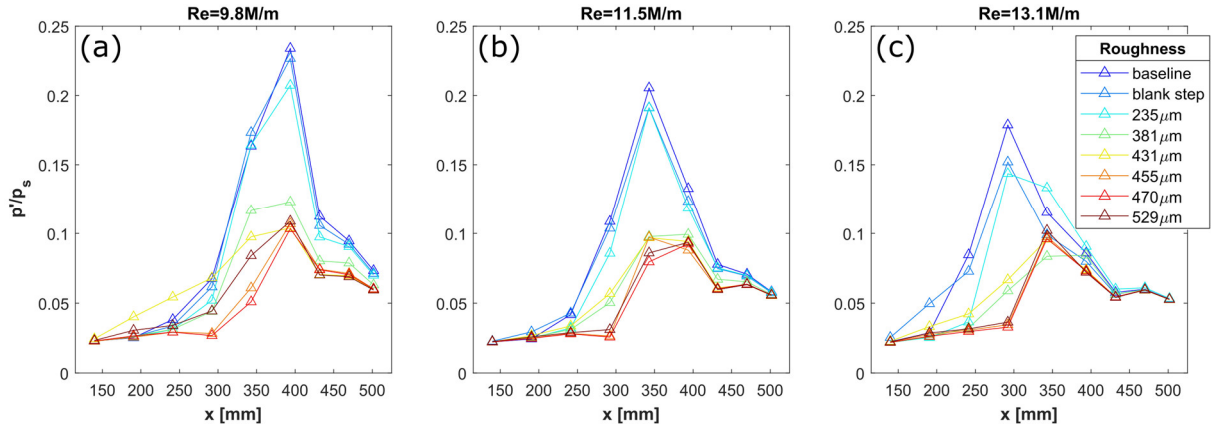
**Figure 15. Axial development of rms pressure fluctuations from PCB® and Kulite® sensors along the 180°
ray for three unit Reynolds numbers (a–c) and six VG heights.**

The axial development of the second-mode and lower-frequency content as a fraction of the full spectral rms for
PCBs® on the 180 deg ray is plotted in Fig. 16. Lower-frequency points below x = 292 mm are again omitted on all
three Reynolds number subplots to reduce line crossings. These plots are similar to those for the 90 deg ray in Fig. 12
and show that the second-mode instability growth is reduced by all roughness arrays, and second-mode amplitudes
recover to a lesser extent downstream of taller VGs. Although taller roughness elements lead to a reduced second
mode, much energy is concentrated in the lower-frequencies, and earlier turbulence is observed.
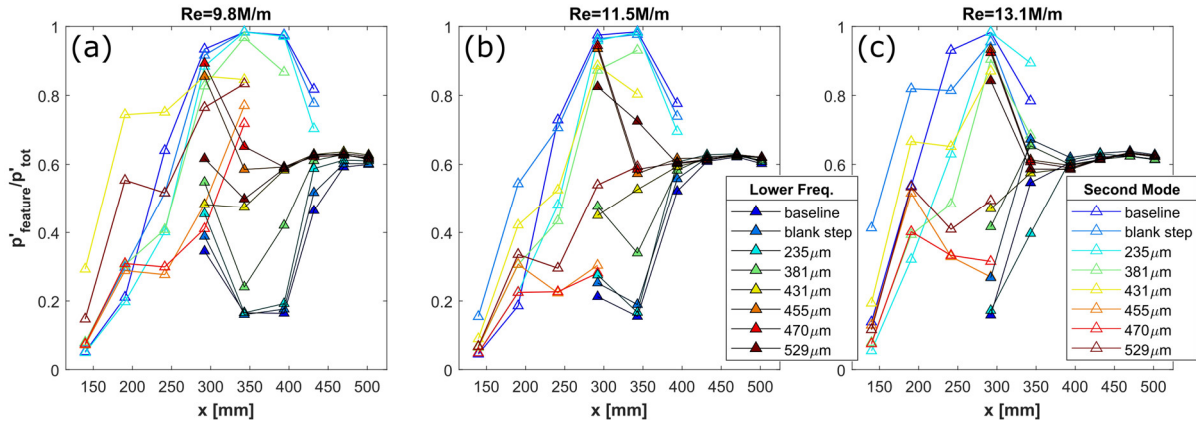

**Figure 16. Axial development of second-mode and lower-frequency rms as a fraction of full PCB®-
bandwidth rms along the 180° ray for three unit Reynolds numbers (a–c) and six VG heights.**

C. Other Roughness

Tests were conducted using arrays of triangular and trapezoidal elements of similar height to compare with the
elliptical VG results. Axial development of Stanton number is plotted in Fig. 17. The subplots are organized by unit
Reynolds number (columns) and azimuthal angle (rows). The profiles on the 90 deg ray show the trapezoidal elements
(green squares) as the clear first to transition onset with large jumps in Stanton number between x = 203 mm and x =
254 mm. The triangular elements (cyan squares) show the second highest increase between those stations. No such
evidence of early transition onset is found on the 180 deg ray, where trapezoidal (green triangles) and triangular (cyan
triangles) elements show some of the lowest Stanton numbers for all Reynolds numbers in the group through x = 305
mm. The reason for the discrepancy in the instability and transition behavior between the 90 and 180 deg rays for the
triangular and trapezoidal roughness is unclear. The differences in location for transition onset and fully turbulent flow
between rays appear larger than the less than 50.8 mm previously observed for other cases.
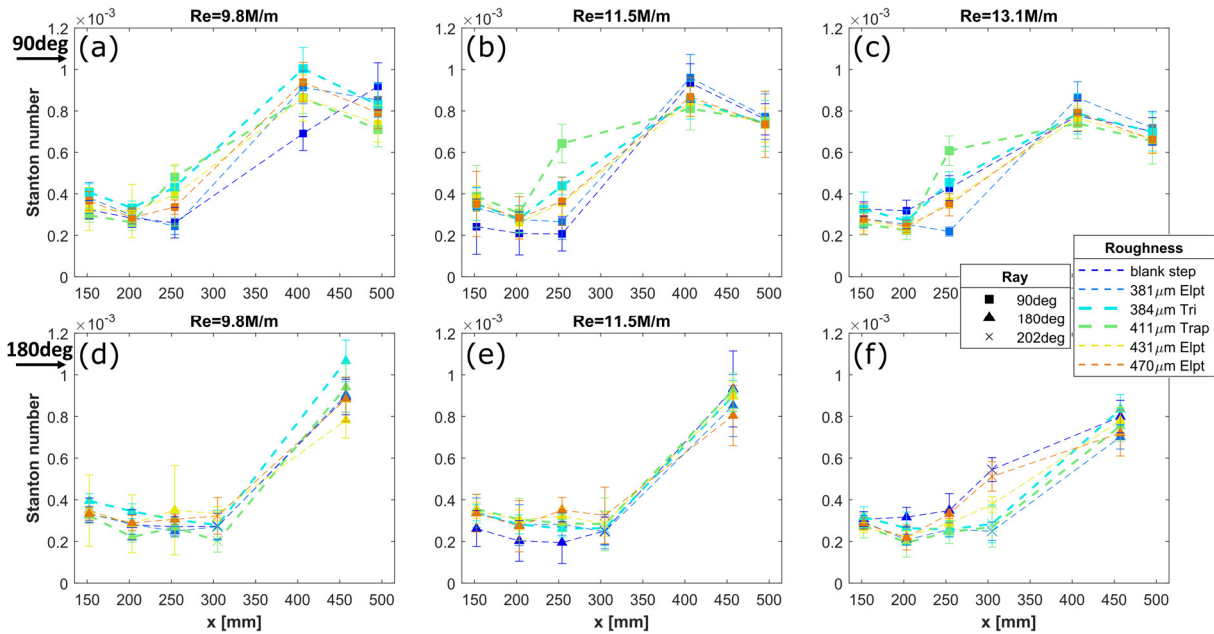
Figure 17. Axial development of Stanton number along the 90° ray (a–c) and near the 180° ray (d–f) for triangular, trapezoidal, and elliptical VGs at three unit Reynolds numbers.

Spectra from the first four 90 deg PCB® and Kulite® sensors downstream of the roughness strip and tested at Re = 11.5 M/m are presented in Fig. 18. The spectra at x = 241 mm (Fig. 18a) suggest that the triangular array reduces the second mode further than any of the elliptical arrays tested, and evidence of second mode is essentially eliminated with the trapezoidal VGs. The next station downstream (Fig. 18b) shows that these VGs generate higher-amplitude low-frequency content than all of the elliptical roughness. By x = 343 mm, the triangular and trapezoidal element spectra appear turbulent as do the spectra from the taller elliptical VGs. Again, there is some mismatch on the Kulite® and PCB® spectra overlapping frequencies, and this is believed to be caused by azimuthal differences in Kulite® and PCB® sensor locations in relation to the individual roughness elements. The spectral trends from the Re = 9.8 and 13.1 M/m cases (not shown here) are similar, except the triangular element spectra are not elevated at lower frequencies for the 9.8 M/m condition at x = 292 mm. However, similar to Re = 11.5 M/m, both the triangular and trapezoidal spectra appear turbulent at x = 343 mm.
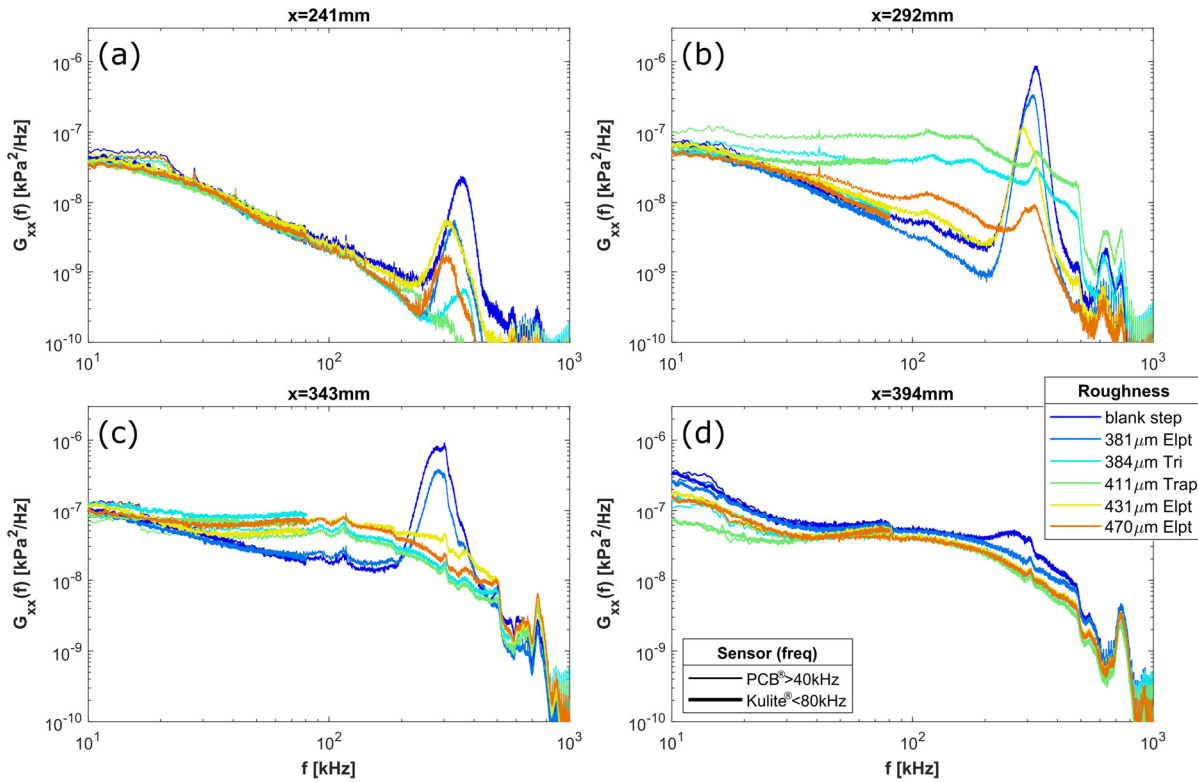
Figure 18. PCB® and Kulite® pressure fluctuation spectra at four streamwise stations (a–d) on the 90° ray for triangular, trapezoidal, and elliptical roughness at Re = 11.5 M/m.

The PSDs for the triangular and trapezoidal elements on the 180 deg ray (Fig. 19) are drastically different. The second mode is not reduced to the same extent as for the 90 deg ray. Large second-mode peaks exist for both new cases at x = 343 mm (Fig. 19c), whereas the spectra were turbulent at this location on the 90 deg ray. The low-frequency content is not broadly elevated at x = 292 mm as it was on the 90 deg ray; instead, PSD values are even below the baseline case at x = 343 mm. All spectra at x = 394 mm (Fig. 19d) are nearly turbulent, with the baseline case remaining the most transitional. Similar observations are made for the Re = 9.8 and 13.1 M/m spectra that are not shown here.
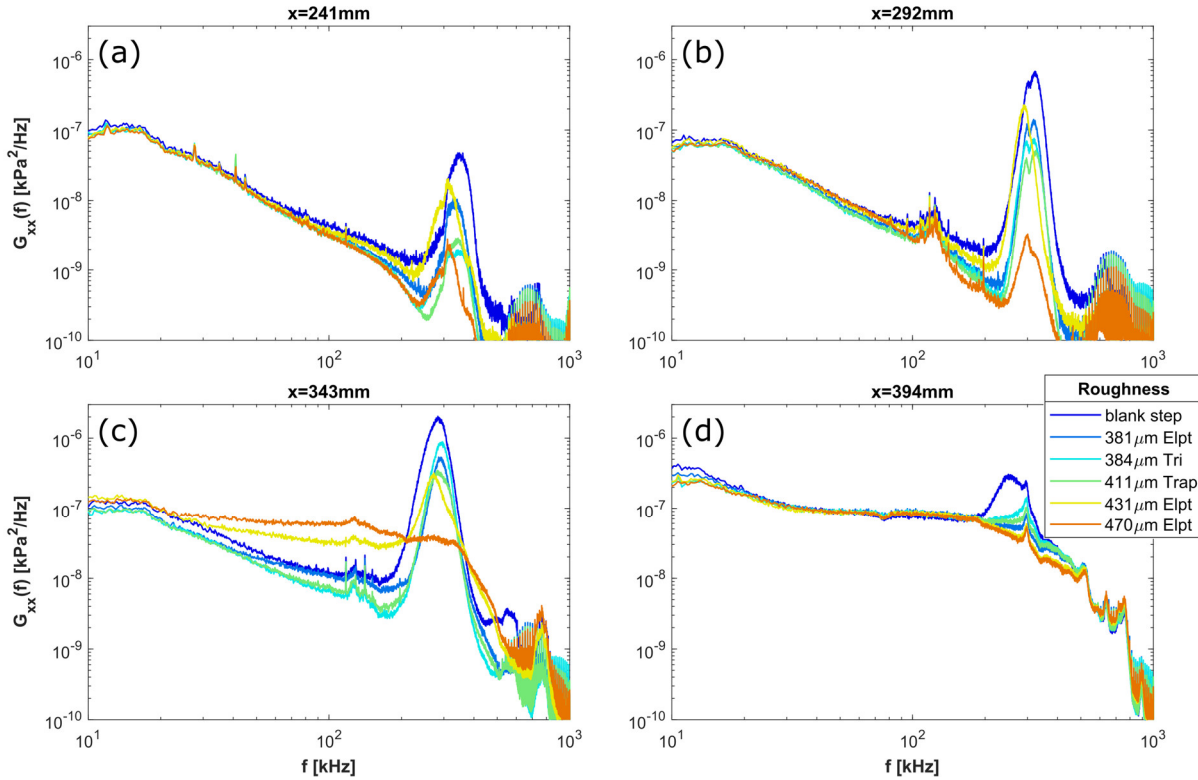
Figure 19. PCB® pressure fluctuation spectra at four streamwise stations (a–d) on the 180° ray for triangular, trapezoidal, and elliptical VGs at Re = 11.5 M/m.

The axial evolution of the rms fluctuations for PCBs® and Kulites® near the 90 deg ray and PCBs® on the 180 deg ray are plotted in Fig. 20. The subplots are organized by unit Reynolds number (columns) and azimuthal angle (rows). The axis scales for the normalized fluctuations are 0.16 and 0.25 for the 90 and 180 deg rays, respectively. The triangular and trapezoidal roughness element lines are bolded for clarity in cyan and green, respectively. The 90 deg PCB® profiles in Figs. 20b and 20c indicate that the fluctuations caused by the triangular and trapezoidal VGs generally increase more between x = 241 mm and x = 292 mm than those caused by the other roughness types. The second-mode peak is almost nonexistent in any of the PCB® PSDs, so the bulk of the RMS fluctuations come from low-frequency disturbances. Since that is the case, it would be expected that the Kulite® rms profiles would mirror the PCB® profiles, but there are some differences due to the high azimuthal variation in low-frequency content. Despite those differences, the PCBs® and Kulites® rms profiles on the 90 deg ray both suggest similar positions of fully turbulent flow for each respective roughness type and flow condition.

The 180 deg rms pressure fluctuation triangular and trapezoidal VG profiles look much different than those on the 90 deg ray because the second-mode peak is a prominent feature on the 180 deg ray. Comparing between the rays suggests that higher-amplitude second-mode peaks correspond with higher rms fluctuation levels and locations of maximum rms that are farther downstream. The triangular and trapezoidal profiles also look more like the elliptical profiles on the 180 deg ray.
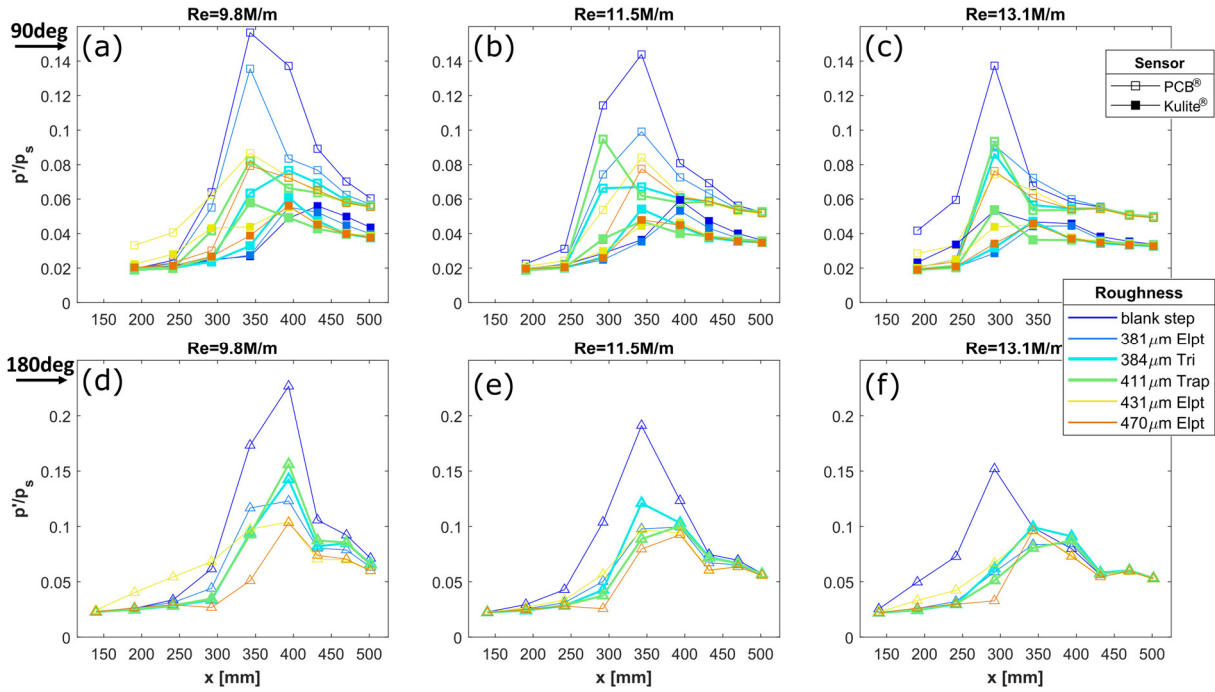
**Figure 20. Axial development of rms pressure fluctuations from PCB® and Kulite® sensors along the 90°
ray (a–c) and from PCB® sensors along the 180° ray (d–f) for triangular, trapezoidal, and elliptical VGs at
three unit Reynolds numbers.**

The differences between the 90 and 180 deg rays are magnified in the feature-specific pressure fluctuation profiles
shown in Fig. 21. The subplots are arranged in the same way as in Fig. 20. The symbols are the same for the second
mode fraction as they were for the PCBs in Fig. 20, while the lower-frequency fraction symbols are the same but are
outlined in black. Lower-frequency points below x = 292 mm are omitted on all subplots to reduce line crossings. A
general observation is that there are far fewer points plotted on the 90 deg subplots than the 180 deg subplots, meaning
the second mode was detected less frequently on the 90 deg ray. This is consistent with the second-mode suppression
observed in the spectra. The second-mode peak remains a prominent feature on the 180 deg ray subplots and persists
to nearly the same location as the blank roughness. As expected, the lower-frequency content is correspondingly high
over most of the model on the 90 deg ray and shows levels comparable to the elliptical roughness on the 180 deg ray.
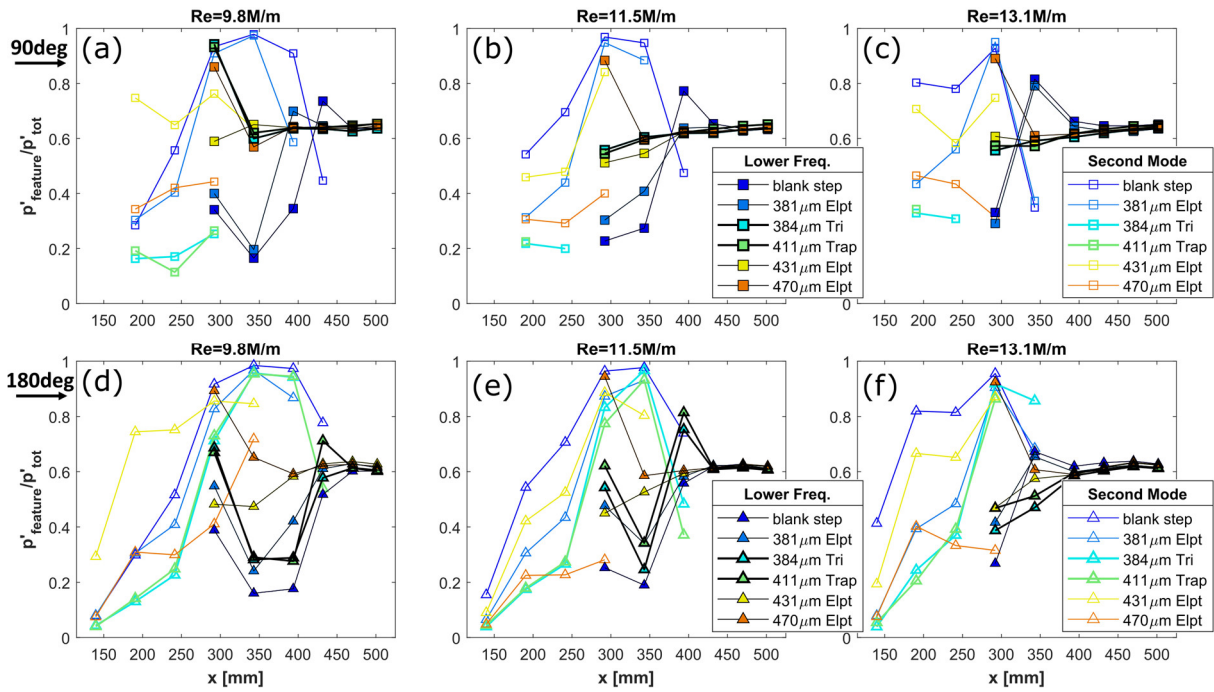
American Institute of Aeronautics and Astronautics

Figure 21. Axial development of second-mode and lower-frequency rms as a fraction of full PCB®-bandwidth rms along the 90° ray (a–c) and along the 180° ray (d–f) for triangular, trapezoidal, and elliptical VGs at three unit Reynolds numbers.

IV. Computations

A. Methods

The basic state corresponding to the laminar boundary layer flow over the cone surface was computed using a second-order accurate algorithm as implemented in the finite-volume compressible Navier-Stokes flow solver VULCAN-CFD [36]. The VULCAN-CFD solution is based on the full Navier-Stokes equations and uses the solver's built-in capability to iteratively adapt the computational grid to the shock. The freestream velocity (926 m/s), density (0.0524 kg/m³), and temperature (59.7 K) and the model wall temperature (304 K) were input based on experimentally measured values for the Re = 11.5 M/m test condition. However, Sutherland's law was used as the viscosity model, which will lead to some differences between the computations and experiments at these relatively low freestream temperatures.

The computational grid used to compute the axisymmetric baseline flow in the absence of any VGs included a total of 1345 points along the axis of the cone and 513 points along the surface-normal direction. The boundary layer profiles near x = 160 mm were used as the inflow condition to compute the azimuthally modulated flow in the presence of the VGs. Similar to the earlier analysis for the HIFiRE-1 flight condition [29], a higher-order accurate code [37] (typically used for direct numerical simulations of transitional and turbulent flows) was used to compute this fully three-dimensional flow. The computational mesh used for this purpose has 1111 points in the axial direction which were clustered in the vicinity of the VGs, whereas a uniform but sufficiently fine grid of 192 points was employed to resolve a single azimuthal wavelength of the periodic VG pattern. A total of 257 points were used to discretize the surface normal domain, which was limited to the region below the shock emanating just upstream of the nose of the cone. A coarser grid with 1.5 times fewer points in each direction was used to verify that the solution features of interest were insensitive to the grid resolution. The modulated basic state computed in this manner was used to predict the effects of the VG pattern on the amplification of both first-mode and second-mode (i.e., Mack mode) instabilities along the cone.

As described in the earlier analysis [29], linear, plane-marching PSE are used to predict the linear amplification characteristics of both modulated Mack-mode waves and the first-mode waves that are found to become the streak-instability waves sustained by finite amplitude streaks induced by the VGs. Similar hypersonic 7 deg half angle cone computations have already been performed in Refs. 29, 38, and 35. Reference 39, additionally, describes the effects of streamwise streaks on first-mode waves for a supersonic boundary layer. Each roughness array for the present experiment had an azimuthal wavenumber of 112 elliptical roughness element pairs. The most unstable streak-instability mode corresponds to the azimuthally subharmonic mode, m = 56.

Similar to Ref. 29, the onset of laminar-to-turbulent transition is estimated computationally using the logarithmic amplification ratio, the so-called N-factor, based on Mack's energy norm and relative to the lower bound location where the disturbance first becomes unstable. A comparison will be made with experimental results for two elliptical planform roughness heights in Section V.

B. Results

Figure 22 displays the crossplane contours of the mean u-velocity at six x locations for elliptical planform VGs with heights of 382 μm (Fig. 22a) and 529 μm (Fig. 22b). These maps allow a side-by-side comparison of the overall disturbance structure at different VG heights. The x = 225 mm location is just upstream of the VGs (centered at x = 229 mm), and the velocity contours at that location indicate virtually no effect of the roughness on the mean flow. Significant flow distortion is observed just downstream of both VG arrays, as seen from the velocity contours at x = 235 mm. Not surprisingly, the taller roughness array leads to a stronger downwelling of high-velocity fluid near the center of the plot, i.e., directly downstream of the converging gap between the roughness elements within each pair of VGs (recall the VG configuration in Fig. 4). Analogously, the significant increase in boundary layer thickness along the sides of each plot indicates that the taller VG array also induces an increased upwelling on the diverging side. For both VG heights, the spanwise gradients associated with the wake distortion decays with downstream distance and a minimal distortion is observed toward the aft end of the cone for the 382 μm VGs. For the 529 μm VGs, on the other hand, one clearly observes a modest distortion in the velocity contour at x = 500 mm.

To further illustrate the axial evolution of the wake flow and its dependence on the VG height, Fig. 23 shows the streak amplitude as a function of x. As defined by Fransson et al. [40], the streak amplitude, A, is the largest variation of the streamwise velocity within a cross section corresponding to a given streamwise location:

$$A(\xi) = \frac{1}{2u_\infty} \max_\eta (\max_\zeta(u) - \min_\zeta(u)) \tag{2}$$

where ξ is the streamwise coordinate, η is the wall-normal coordinate, ζ is the azimuthal coordinate, and u is the streamwise velocity component. Streak amplitudes reach maximum values just downstream of the roughness elements, with $A = 0.1054$ at x = 237.3 mm for the 382 µm VGs and $A = 0.2014$ at x = 242.5 mm for the 529 µm VGs. Streak-amplitude values decrease downstream for the remainder of both profiles. At the end of the cone, the amplitude for the 529 µm roughness is 0.066, more than triple the value of the shorter elements.
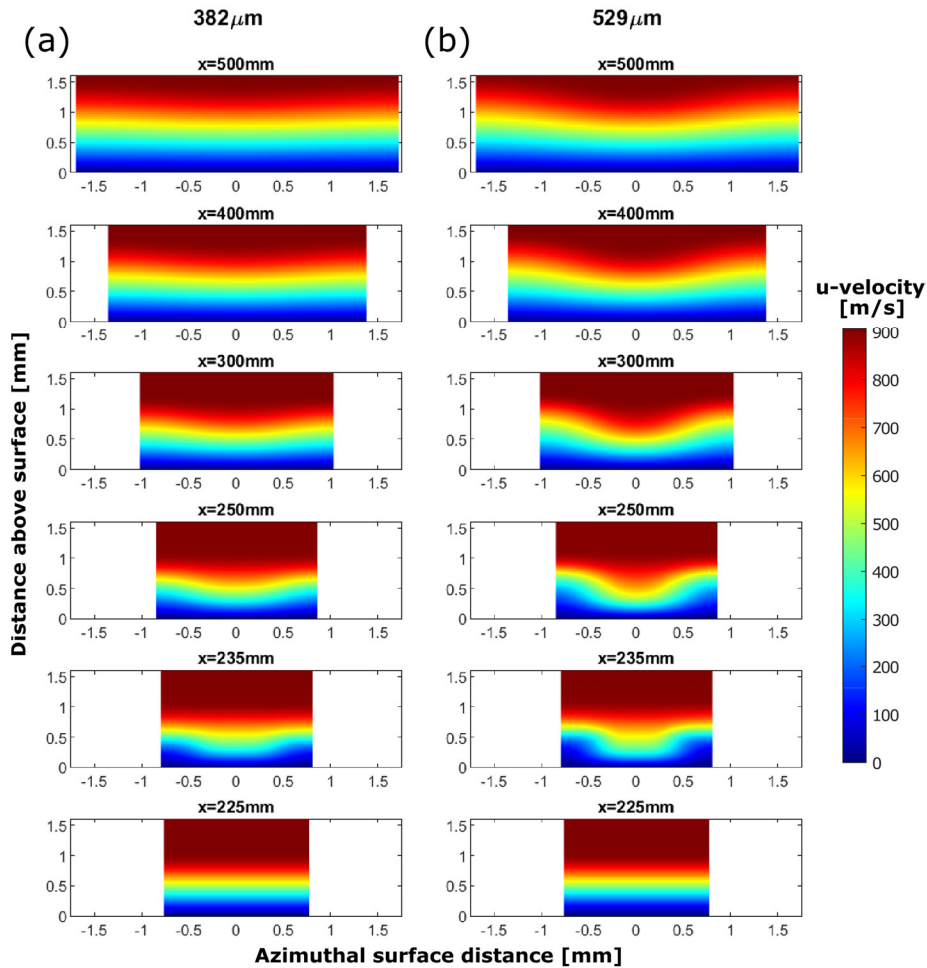

Figure 22. Predicted mean u-velocity contours at six different streamwise-normal slices above the cone for (a) 382 µm and (b) 529 µm roughness heights (Re = 11.5 M/m).
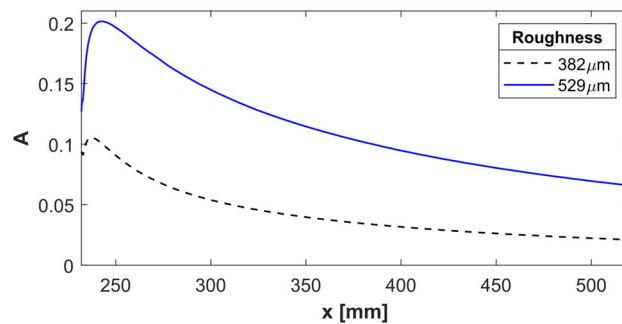

Figure 23. Predicted streak amplitude for 382 µm and 529 µm elliptical roughness elements.

American Institute of Aeronautics and Astronautics

N-factors curves based on Mack's energy norm (as defined in Ref. 35) for the unperturbed flow are plotted in Fig. 24. The second-mode curves, shown in Fig. 24a, demonstrate the trend of higher-amplitude, lower-frequency waves with increasing axial location. The most amplified frequency at x = 229 mm is 380 kHz. The envelope encompassing all frequencies shows that the amplitudes grow quickly on this model at the test condition corresponding to Re = 11.5 M/m, and the N-factors reach a peak value of nearly nine by the end of the cone. The N-factor curves for the oblique first-mode instability waves are shown in Fig. 24b. Each frequency curve represents an envelope of relevant azimuthal wavenumbers (m between 10–60), and the full envelope of all frequencies and wavenumbers is displayed as the thicker black curve. The first-mode N-factors are lower and grow more slowly than the second-mode N-factors. A wider range of frequencies are observed near the envelope in comparison to the second mode, particularly near x = 229 mm, where similar N-factor values are observed for frequencies between 50–120 kHz.
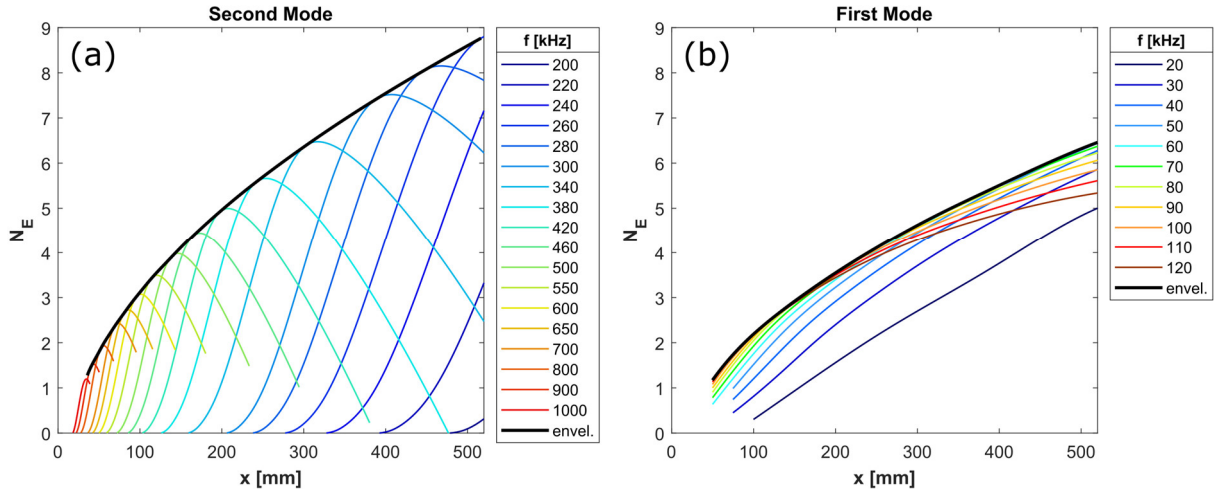

Figure 24. N-factor plots for (a) second-mode and (b) oblique first-mode envelopes for relevant azimuthal wavenumbers. The overall envelopes are shown with thick black lines.

Second-mode N-factor curves for the 382 μm and 529 μm roughness height cases are shown in Fig. 25. The VGs significantly reduce the second-mode N-factors for both heights, especially just downstream of the array. This finding is similar to that in Ref. 38, where the mean flow modulation was associated with optimal growth disturbances. For 382 μm VGs (Fig. 25a), N-factor values between 340–360 kHz are reduced by around one. The second mode recovers for x > 300 mm, and the N-factors for f < 320 kHz exceed the unperturbed baseline envelope. For 529 μm (Fig. 25b), the second mode is further reduced at all locations downstream of the roughness. N-factors are reduced by 2 between 340–360 kHz. N-factors for these frequencies are reduced to such an extent that the 300 kHz curve has the highest N-factors between x = 298–368 mm, whereas the same curve is highest for x = 340–412 mm and x = 367–417 mm for the 382 μm height and baseline cases, respectively. The second mode does recover on the downstream portion of the model, but not to the level of the shorter elements as the baseline N-factor envelope is never reached within the computational domain.
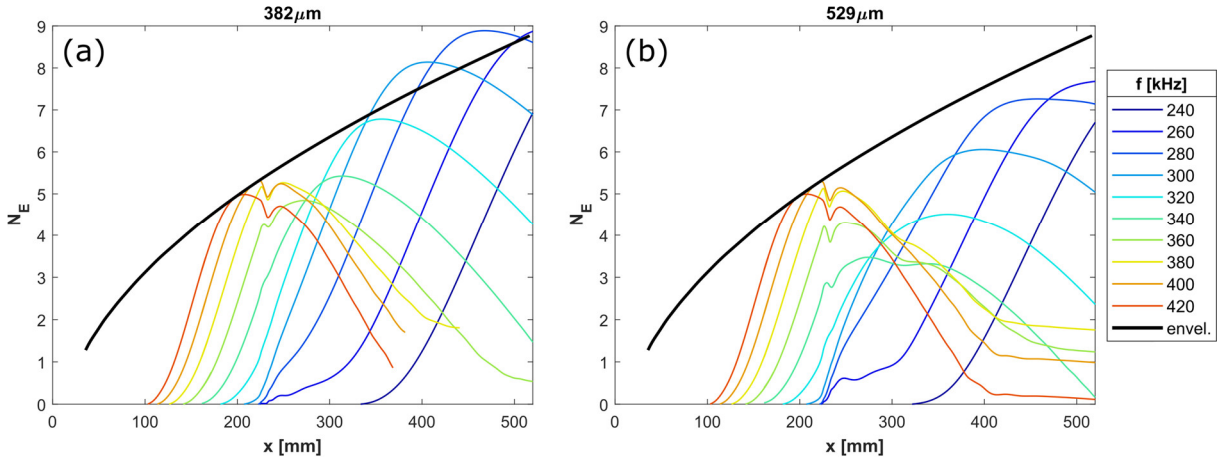
Figure 25. Second-mode N-factors for (a) 382 μm and (b) 529 μm roughness heights. The baseline envelope is represented by the thick black lines.

N-factor curves for the m = 56 first mode waves, which become the streak instability waves downstream of the VGs, for both roughness heights are shown in Fig. 26. The first-mode envelope, representing the envelope for all frequencies in Fig. 24 is shown in bolded black. The streak-instability results correspond to the azimuthally subharmonic sinuous mode that is the most amplified by the streaks as in Ref. 29, and is found to emanate from the first mode upstream of the VGs with the same azimuthal wavelength, m = 56. For both element heights and all frequencies, the VGs initially cause the N-factor to dip, but the reduction is slight in comparison to the second mode. The streak-instability growth is then accelerated compared to the baseline envelope of azimuthal wavenumbers and frequencies. The N-factors do not overtake the overall baseline envelope at any point for the 382 μm VGs, but they do at x = 347 mm for the 529 μm VGs.
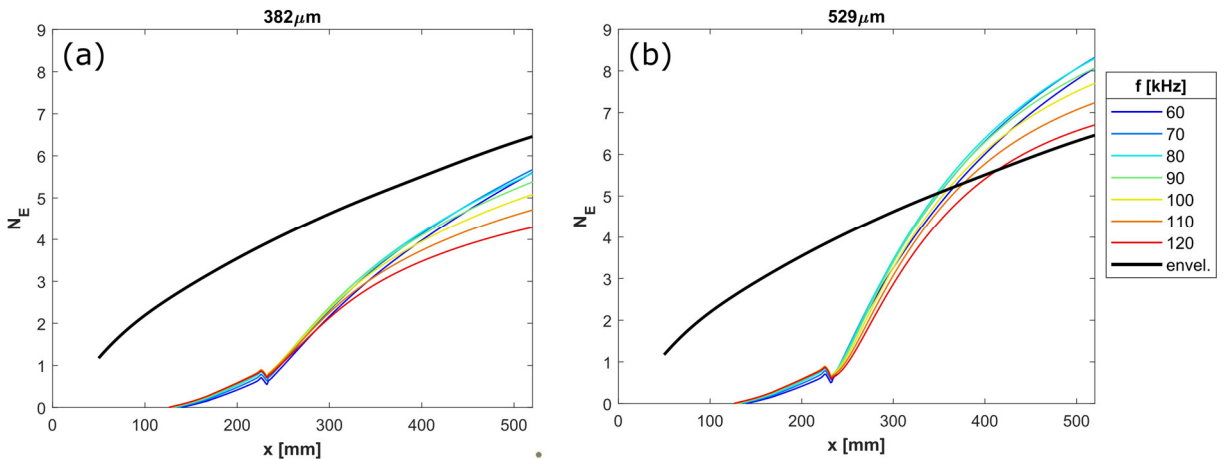

Figure 26. Streak-instability (m = 56) N-factors for (a) 382 μm and (b) 529 μm roughness heights. The baseline first-mode envelope for all azimuthal wavenumbers and frequencies is represented by the thick black lines.

V. Discussion

The stability results obtained from the computations are consistent with and helpful in interpreting the measurements acquired from the experiments. The PCB® pressure transducers enabled the measurement of the second-mode instability along the length of the cone and the spectra were calculated for each axial location. Although the transducers only provided point measurements and the precise transition locations could not be ascertained, the

measurements gave insight into the nature of the instability evolution and the transition mechanism. For the baseline Re = 11.5 M/m case, the PCBs® (Fig. 6) indicate a maximum second-mode amplitude near x = 343 mm, with a frequency peak around 300 kHz. The predicted value of the peak second-mode N-factor (Fig. 24) at the same x location is 320 kHz. As mentioned earlier, discrepancies may be caused by the difference in the viscosity model. Use of Sutherland viscosity for the CFD yields a higher Reynolds number, lower boundary layer thickness, and a higher frequency for the instability. The pressure transducers and thermocouples suggest the onset of transition is also near x = 343 mm (Figs. 5–7). The corresponding maximum second-mode N-factor at that axial location is 6.9. The first-mode N-factor is just above 5.

PCBs® on both the 90 deg (Fig. 9) and 180 deg (Fig. 14) rays demonstrate a reduction in the second mode downstream of the 381 μm elliptical roughness elements, without an immediate corresponding elevation of lower-frequency content. The spectra show a more severe reduction in the second mode for 529 μm roughness, and the spectra also broaden farther upstream. For both roughness heights, the second-mode peak shifts to lower frequencies with respect to the baseline case, most notably for the PCB® located closest to the roughness (x = 241 mm). On the 90 deg ray (Fig. 9a), the frequency for the maximum PSD value of the second mode shifts from 367 kHz for the baseline, to 330 kHz for the 381 μm VG case, and to 308 kHz for the 529 μm VG case. The 180 deg ray (Fig. 14a) gives a similar frequency shift with roughness height, but the second-mode amplitude is further reduced along this ray for the 529 μm case, obscuring a clear peak. The baseline CFD (Fig. 24a) shows the 380 kHz curve with the maximum second-mode N-factor at x = 241 mm, again giving a slightly higher frequency than the experiments. Interestingly, roughness computations (Fig. 25) do not show the higher-frequency second-mode N-factor curves as being significantly reduced by x = 241 mm. Instead, the major curve reduction takes place farther downstream computationally, with the largest reduction from the baseline envelope located near the position of the next PCB® at x = 292 mm. The PCBs®, however, show the frequency offsets between the peaks closing and virtually no difference in frequency of the spectral peaks at the x = 343 mm station (Figs. 9c and 14c). After the initial reduction in second-mode amplitude at x = 241 mm, the 381 μm experimental spectra showed a substantial rebound for the instability, but the 529 μm case only made a marginal recovery before the second mode disappeared entirely at x = 343 mm. The second-mode N-factor plots confirm this behavior, first by showing that the second mode reduces further for taller roughness and that the renewed increase in N-factor downstream of the local minimum in the N-factor envelope is also reduced at the larger roughness height.

In terms of lower-frequency content, the PCB® spectra for the case of 381 μm VGs trend with the baseline on both rays, while the PSDs for the 529 μm roughness case deviate almost immediately downstream of the VGs at x = 241 mm on the 90 deg ray (Fig. 9a) and x = 292 mm on the 180 deg ray (Fig. 14b). The predicted N-factors of the streak instability (Fig. 26) are sufficiently low in the 381 μm case, so that the N-factor envelope in the first-mode range is predicted to remain the same as the baseline case. On the other hand, the computational predictions for the 529 μm roughness case are only partially consistent with the experimental observation in that the streak-instability N-factors do exceed the first-mode growth in the baseline case, but this excess growth is manifest farther downstream in comparison with the excess growth observed in the experiments at x = 241 mm (90 deg ray) and x = 292 mm (180 deg ray).

The computations provide explanations for the observed differences in spectra between PCBs® on the 90 and 180 deg rays and the differences in lower-frequency PSD values between the PCBs® and corresponding azimuthally offset Kulites®. Significant mean flow distortion is observed in Fig. 22, and the streak amplitudes plotted in Fig. 23 demonstrate that differences persist down the length of the cone, particularly for taller roughness elements. Although not shown in the present manuscript, significant crossplane variation was also observed in the instability analysis. We also note that the VGs used in the experiment are likely to have small but significant variations across the azimuthal extent of the array, resulting in similar variations in the flow distortion in the wake of the VG array, and hence, in the amplitudes of the unsteady disturbances at any given axial location.

Ultimately, the experiment indicates that reducing the second-mode amplitude with VGs did not generally result in a measurable delay in transition. There is limited evidence that the onset of transition may have been delayed for shorter elliptical 235 μm and 381 μm cases at 13.1 M/m. For those cases, the first measured increase in Stanton number was farther downstream than the baseline case (Figs. 8c and 13c), and the lower-frequency pressure fluctuation PSD values were below the baseline levels (Fig. 10a). Evidence for delayed transition is also supported by the spectrum for the 235 case (Fig. 10b), which indicates a delayed transitional state versus the baseline case as evidenced by the larger remnant of the second-mode instability. Unfortunately, the sparsity of thermocouples prevents a clear quantitative definition of the transitional range.

The data show that the second-mode instability was no longer the transition mechanism for cases with taller VGs. The second-mode amplitudes for those cases were never able to reach the pretransitional amplitudes attained over the smooth cone; instead, the lower-frequency content increased appreciably, and the first-mode or streak instability most

likely became the dominant transition mechanism. Although the streak instability N-factors in Fig. 26 are relatively low, the experiments took place in a conventional facility. The elevated disturbance environment combined with the three-dimensional roughness often led to earlier transition for the larger roughness elements. Thus, transition could be delayed in a low-disturbance quiet facility, where tunnel noise would contribute minimally to the streak disturbances, and the second mode would likely be the transition mechanism. The above observations underscore the limitations of transition measurements in conventional facilities, as not only the initial disturbance amplitudes but even the transition mechanism can be altered by the facility disturbances.

VI. Conclusion

An experimental campaign was performed in the 20-Inch Mach 6 Wind Tunnel to test the effect of shaped roughness elements on boundary layer transition to turbulence for a 7 degree half-angle cone. Elliptical planform elements were sized based on guidance from previous computations for other high-speed configurations. The matrix included testing different height elliptical element arrays as well as triangular and trapezoidal element arrays. These configurations were tested at five different Reynolds numbers, but the primary focus was on the Re = 11.5 M/m condition. High-bandwidth PCB® pressure transducers located downstream of the VGs demonstrated that the second-mode instability was generally further reduced with taller roughness elements. However, this coincided with a spectral shift to lower frequencies and generally led to earlier boundary layer transition, contrary to expectations. Nevertheless, there is some evidence that transition may have been delayed for shorter elliptical VGs at the Re = 13.1 M/m condition.

Complementary computations were performed to help interpret the experimental results. Stability analysis was performed on the model with 382 µm and 529 µm elliptical planform roughness arrays. The energy norm N-factors demonstrated significant reduction in the second mode, particularly for the first 100δ downstream of the roughness array. The N-factors for the most unstable first mode (m = 56) that became the subharmonic streak instability mode were observed to increase relative to the baseline envelope of azimuthal wavenumbers and frequencies, but only exceeded the envelope for the 529 µm height. With consideration that the experiments took place in a conventional tunnel, it can be concluded that the elevated freestream disturbances interacted with the streak instabilities to induce earlier transition at the larger roughness height.

References

[1] Arnal, D. and Archambaud, J. P., "Laminar-Turbulent Transition Control: NLF, LFC, HLFC," Advances in Laminar-Turbulent Transition Modeling, AVT-151 RTO AVT/VKI, Lecture Series, von Kármán Institute for Fluid Dynamics, Rhode St. Genèse, Belgium, 2009.

[2] Van Driest, E. R., "The Problem of Aerodynamic Heating," *Aeronautical Engineering Review*, Vol. 15, No. 10, 1956, pp. 26–41.

[3] Schneider, S. P., "Hypersonic Laminar-Turbulent Transition on Circular Cones and Scramjet Forebodies," *Progress in Aerospace Sciences*, Vol. 40, Nos. 1–2, 2004, pp. 1–50. doi.org/10.1016/j.paerosci.2003.11.001

[4] Stetson, K. F., "Comments on Hypersonic Boundary Layer Transition," WRDC-TR-90-3057, Sept., 1990.

[5] Mack, L. M., "Boundary-Layer Linear Stability Theory," Special Course on Stability and Transition of Laminar Flow, AGARD Rept. 709, Neuilly-Sur-Seine, France, 1984, pp. 3-1–3-81.

[6] Marineau, E. C., Moraru, C. G., and Daniel, D. T., "Sharp Cone Boundary-Layer Transition and Stability at Mach 14," *55th AIAA Aerospace Sciences Meeting*, AIAA Paper 2017-0766, 2017. doi.org/10.2514/6.2017-0766

[7] Marineau, E. C., Moraru, G. C., Lewis, D. R., Norris, J. D., Lafferty, J. F., and Johnson, H., "Investigation of Mach 10 Boundary

Layer Stability of Sharp Cones at Angle-of-Attack, Part 1: Experiments," *53rd AIAA Aerospace Sciences Meeting*, AIAA Paper 2015-1737, 2015. doi.org/10.2514/6.2015-1737

[8] Marineau, E. C., Moraru, C. G., Lewis, D. R., Norris, J. D., Lafferty, J. F., Wagnild, R. M., and Smith, J. L., "Mach 10 Boundary-Layer Transition Experiments on Sharp and Blunted Cones," *19th AIAA International Space Planes and Hypersonic Systems and Technologies Conference*, AIAA Paper 2014-3108, 2014. doi.org/10.2514/6.2014-3108

[9] Wadhams, T., MacLean, M., Parker, R., and Holden, M, "Evaluation of Boundary Layer Transition on a Large Sharp 7-degree Cone at Mach 10 over a Range of Velocities and Reynolds Numbers," *22nd AIAA International Space Planes and Hypersonics Systems and Technologies Conference*, AIAA 2018-5323, 2018. doi.org/10.2514/6.2018-5323

[10] Casper, K. M., Beresh, S. J., Henfling, J. F., Spillers, R. W., Pruett, B. O. M., and Schneider, S. P., "Hypersonic Wind-Tunnel Measurements of Boundary-Layer Transition on a Slender Cone," *AIAA Journal*, Vol. 54, No. 4, 2016, pp. 1250–1263. doi.org/10.2514/1.J054033

[11] Grossir, G., Pinna, F., Bonucci, G., Regert, T., Rambaud, P., andChazot, O., "Hypersonic Boundary Layer Transition on a 7 Degree Half-Angle Cone at Mach 10," *7th AIAA Theoretical Fluid Mechanics Conference*, AIAA Paper 2014-2779, 2014. doi.org/10.2514/6.2014-2779

[12] Wagner, A., Kuhn, M., Martinez Schramm, J., and Hannemann, K., "Experiments on Passive Hypersonic Boundary Layer Control Using Ultrasonically Absorptive Carbon-Carbon Material with Random Microstructure," *Experiments in Fluids*, Vol. 54, No. 10, 2013, pp. 1–10. doi:10.1007/s00348-013-1606-3

[13] Heitmann, D., Radespiel, R., and Knauss, H., "Experimental Study of Boundary-Layer Response to Laser-Generated Disturbances at Mach 6," *Journal of Spacecraft and Rockets*, Vol. 50, No. 2, 2013, pp. 305–316. doi.org/10.2514/1.A32281

[14] Rufer, S. J. and Berridge, D. C., "Experimental Study of Second-Mode Instabilities on a 7-Degree Cone at Mach 6," *41st AIAA Fluid Dynamics Conference and Exhibit*, AIAA Paper 2011-3877, 2011. doi.org/10.2514/6.2011-3877

[15] Berridge, D. C., Casper, K. M., Rufer, S. J., Alba, C. R., Lewis, D. R., Beresh, S. J., and Schneider, S. P., "Measurements and Computations of Second-Mode Instability Waves in Several Hypersonic Wind Tunnels," *40th AIAA Fluid Dynamics Conference and Exhibit*, AIAA Paper 2010-5002, 2010. doi.org/10.2514/6.2010-5002

[16] Tanno, H., Komuro, T., Sato, K., Itoh, K., Takahashi, M., and Fujii, K., "Measurement of Hypersonic High-Enthalpy Boundary Layer Transition on a 7° Cone Model," *48th AIAA Aerospace Sciences Meeting Including the New Horizons Forum and Aerospace Exposition*, AIAA Paper 2010-0310, 2010. doi.org/10.2514/6.2010-310

[17] Estorf, M., Radespiel, R., Schneider, S. P., Johnson, H. B., and Hein, S., "Surface-Pressure Measurements of Second-Mode Instability in Quiet Hypersonic Flow," *46th AIAA Aerospace Sciences Meeting and Exhibit*, AIAA Paper 2008-1153, 2008. doi.org/10.2514/6.2008-1153

[18] Marineau et al. "Analysis of Second-Mode Amplitudes on Sharp Cones in Hypersonic Wind Tunnels," *Journal of Spacecraft and Rockets*, Vol. 56, No. 2, 2019, pp 307–318. doi.org/10.2514/1.A34286

[19] Fujii, K., "Experiment of the Two-Dimensional Roughness Effect on Hypersonic Boundary-Layer Transition," *Journal of Spacecraft and Rockets*, Vol. 43, No. 4, 2006, pp. 731–738. doi.org/10.2514/1.17860

[20] Berridge, D. C., "Generating Low-Pressure Shock Waves for Calibrating High-Frequency Pressure Sensors," PhD dissertation, School of Aeronautics and Astronautics, Purdue University, December 2015.

[21] E. J. Softley, "Boundary Layer Transition on Hypersonic Blunt, Slender Cones," 2nd Fluid and Plasma Dynamics Conference, AIAA Paper 69-0705, 1969. doi.org/10.2514/6.1969-705

[22] Stetson, K. F., Thompson, E. R., Donaldson, J. C., and Siler, L. G., "Laminar Boundary Layer Stability Experiments on a Cone at Mach 8, Part 2: Blunt Cone," *22nd Aerospace Sciences Meeting*, AIAA Paper 84-6, 1984. doi.org/10.2514/6.1984-6

[23] Balakumar, P. and Chou, A., "Transition Prediction in Hypersonic Boundary Layers Using Receptivity and Freestream Spectra," *AIAA Journal*, Vol. 56, No. 1, 2018, pp. 193–208. doi.org/10.2514/1.J056040

[24] James, C. S., "Boundary Layer Transition on Hollow Cylinders in Supersonic Free Flight as Affected by Mach Number and a Screwthread Type of Surface Roughness," NASA TR-Memo-1-20-59A, 1959.

[25] Holloway, P. F., and Sterrett, J. R., "Effect of Controlled Surface Roughness on Boundary-Layer Transition and Heat Transfer at Mach Numbers of 4.8 and 6.0, " NASA TN-D-2054, 1964.

[26] Fong, K. D., Wang, X., Huang, Y., Zhong, X., McKiernan, G. R., Fisher, R. A., and Schneider, S. P., "Second Mode Suppression in Hypersonic Boundary Layer by Roughness: Design and Experiments," *AIAA Journal*, Vol. 53, No. 10, 2015, 3138–3144. doi.org/10.2514/1.J054100

[27] Ma, Y. and Zhong, X., "Receptivity of a Supersonic Boundary Layer over a Flat Plate. Part 1: Wave Structures and Interactions," *Journal of Fluid Mechanics*, Vol. 488, 2003, pp. 31–78. doi.org/10.1017/S0022112003004786

[28] Ma, Y. and Zhong, X., "Receptivity of a Supersonic Boundary Layer over a Flat Plate. Part 2: Receptivity to Freestream Sound," *Journal of Fluid Mechanics*, Vol. 488, 2003, pp. 79–121. doi.org/10.1017/S0022112003004798

[29] Paredes, P., Choudhari, M. M., and Li, F., "Transition Delay via Vortex Generators in a Hypersonic Boundary Layer at Flight Conditions," *2018 Fluid Dynamics Conference*, AIAA Paper 2018-3217, 2018. doi.org/10.2514/6.2018-3217

[30] Berger, K., Rufer, S., Hollingsworth, K., and Wright, S., "NASA Langley Aerothermodynamics Laboratory: Hypersonic Testing Capabilities," *53rd AIAA Aerospace Sciences Meeting*, AIAA Paper 2015-1337, 2015. doi.org/10.2514/6.2015-1337

[31] Chou, A., Leidy, A., King, R. A., Bathel, B. F., and Herring, G., "Measurements of Freestream Fluctuations in the NASA Langley 20-Inch Mach 6 Tunnel," *2018 Fluid Dynamics Conference*, AIAA 2018-3073, 2018. doi.org/10.2514/6.2018-3073

[32] Hollis, B. R., "Real-Gas Flow Properties for NASA Langley Research Center Aerothermodynamic Facilities Complex Wind Tunnels," NASA Contracter Report 4755, September 1996.

[33] Welch, P., "The Use of Fast Fourier Transform for the Estimation of Power Spectra: A Method Based on Time Averaging Over Short, Modified Periodograms," *IEEE Transactions on Audio and Electroacoustics*, Vol. 15, No. 2, 1967, pp. 70–73. doi.org/10.1109/TAU.1967.1161901

[34] Boyd, C. and Howell, A., "Numerical Investigation of One-Dimensional Heat-Flux Calculations," Tech. rep., Naval Surface Warfare Center Dahlgren Div., Silver Spring, MD, 1994.

[35] Paredes, P., Choudhari, M., and Li, F., "Instability Wave-Streak Interactions in a High Mach Boundary Layer at Flight Conditions," *Journal of Fluid Mechanics*, Vol. 858, 2018, pp. 474–499. doi.org/10.1017/jfm.2018.744

[36] Litton, D., Edwards, J., and White, J., "Algorithmic Enhancements to the VULCAN Navier-Stokes Solver," *16th AIAA Computational Fluid Dynamics Conference*, AIAA Paper 2003-3979, 2003. doi.org/10.2514/6.2003-3979

[37] Wu, M. and Martin, M. P., "Direct Numerical Simulation of Supersonic Boundary Layer over a Compression Ramp," *AIAA Journal*, Vol. 45, No. 4, 2007, pp. 879–889. doi.org/10.2514/1.27021

[38] Paredes, P., Choudhari, M., and Li, F., "Transition Delay in Hypersonic Boundary Layers via Optimal Perturbations," NASA/TM-2016-219210, 2016.

[39] Paredes, P., Choudhari, M., and Li, F., "Instability Wave-Streak Interactions in a Supersonic Boundary Layer". *Journal of Fluid Mechanics*, Vol. 831, 2017, pp. 524–553. doi.org/10.1017/jfm.2017.630

[40] Fransson, J. H., Brandt, L., Talamelli, A., and Cossu, C., "Experimental and Theoretical Investigation of the Nonmodal Growth of Steady Streaks in a Flat Plate Boundary Layer," *Physics of Fluids*, Vol. 16, No. 10, 2004, pp. 3627–3638. doi.org/10.1063/1.1773493